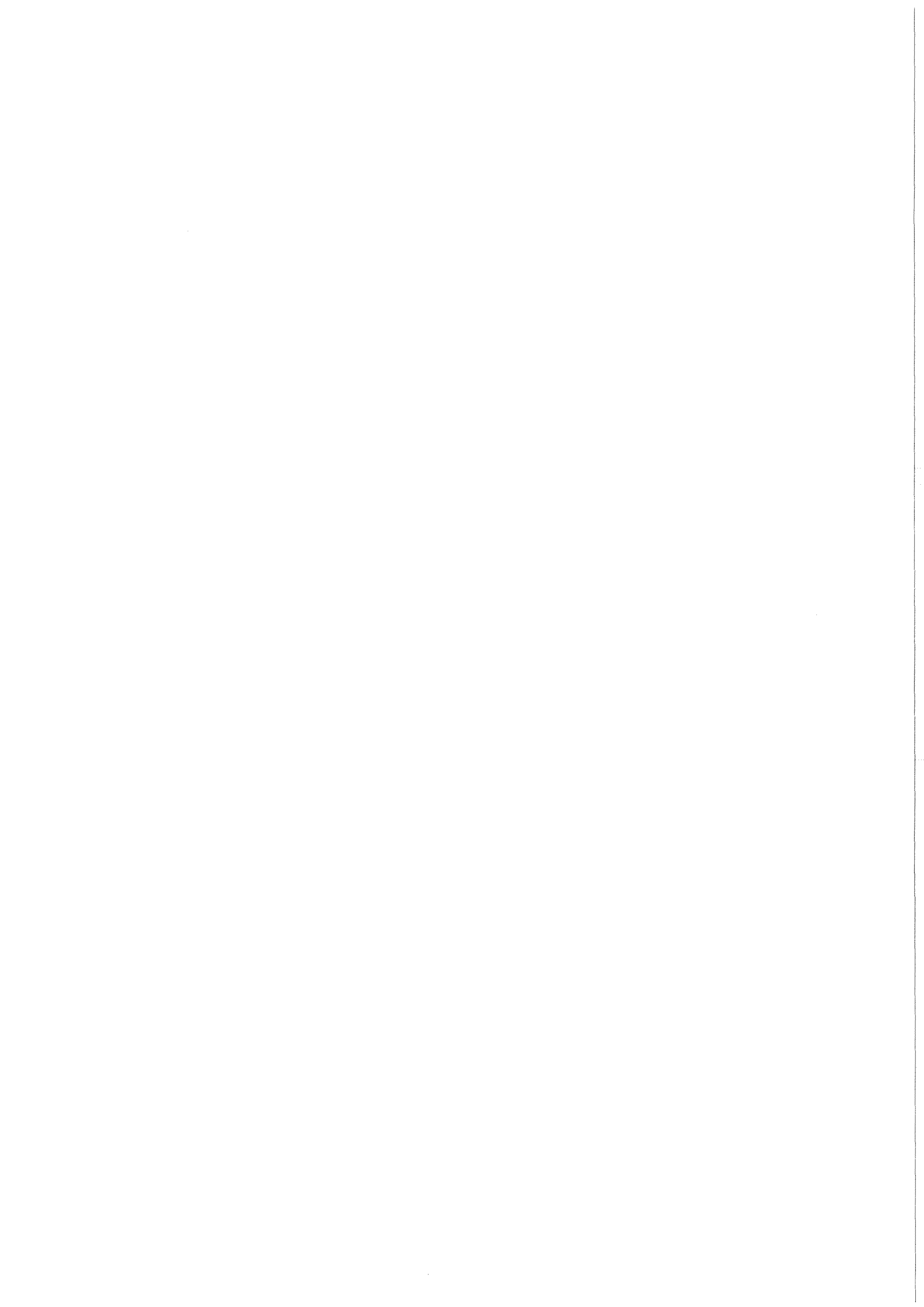# The Structure of Single-phase Turbulent Flows through Closely Spaced Rod Arrays

J. D. Hooper, K. Rehme

Institut für Neutronenphysik und Reaktortechnik

Projekt Schneller Brüter

Kernforschungszentrum Karlsruhe

KERNFORSCHUNGSZENTRUM KARLSRUHE

Institut für Neutronenphysik und Reaktortechnik
Projekt Schneller Brüter

KfK 3467

The structure of single-phase turbulent
flows through closely spaced rod arrays

J. D. Hooper, K. Rehme

Kernforschungszentrum Karlsruhe GmbH, Karlsruhe

Abstract

The axial and azimuthal turbulence intensity in the rod gap region
has been shown, for developed single-phase turbulent flow through
parallel rod arrays, to strongly increase with decreasing rod
spacing. Two array geometries are reported, one constructed from a
retangular cross-section duct containing four rods and spaced at
five p/d or w/d ratios. The second test section, constructed from
six rods set in a regular square-pitch array, represented the
interior flow region of a large array.

The mean axial velocity, wall shear stress variation and axial
pressure distribution were measured, together with hot-wire
anemometer measurements of the Reynolds stresses. No significant
non-zero secondary flow components were detected, using techniques
capable of resolving secondary flow velocities to 1 % of the local
axial velocity. For the lowest p/d ratio of 1.036, cross-corre-
lation measurements showed the presence of an energetic periodic
azimuthal turbulent velocity component, correlated over a signi-
ficant part of the flow area. The negligible contribution of secon-
dary flows to the axial momentum balance, and the large azimuthal
turbulent velocity component in the rod gap area, suggest a diffe-
rent mechanism than Reynolds stress gradient driven secondary
flows for the turbulent transport process in the rod gap.

Die Struktur der einphasigen turbulenten Strömung durch eng gepackte Stabbündel

Zusammenfassung

Für ausgebildete, einphasige turbulente Strömung durch Stabbündel
steigen die axiale und azimutale Turbulenzintensität im Spalt
zwischen den Stäben stark mit sinkendem Stababstand an. Es wird
über zwei Geometrien berichtet, die eine bestehend aus vier
Stäben umschlossen von einem Rechteckkanal für fünf verschiedene
p/d bzw. w/d Verhältnisse. Die zweite Teststrecke aus sechs Stäben
in einer quadratischen Anordnung stellt die innere Strömungszone
einer großen Anordnung dar.

Gemessen wurden die mittlere Axialgeschwindigkeit, Wandschubspan-
nungs- und axiale Druckverteilungen, sowie die Reynolds'schen
Spannungen mithilfe von Hitzdraht-Anemometern. Signifikante
Sekundärströmungen wurden nicht festgestellt mit einer Methode,
die Sekundärströmungen von 1% der örtlichen Axialgeschwindigkeit
zu ermitteln gestattet. Für das kleinste p/d-Verhältnis von 1.036
zeigten Kreuzkorrelationsmessungen, daß eine energetische azimu-
tale periodische Geschwindigkeitskomponente über einen größeren
Teil des Strömungsquerschnitts auftritt. Der vernachlässigbare
Beitrag von Sekundärströmungen zur Impulsbilanz in axialer Richtung
und die starke azimutale Geschwindigkeitskomponente im Spalt
zwischen den Stäben deuten auf einen anderen Mechanismus für den
Turbulenztransport im Spalt hin als Sekundärströmungen aufgrund
von Gradienten der Reynolds'schen Spannungen.

1. Introduction

Fully developed single phase turbulent flow through closed
straight non-circular ducts is helical in nature. The spiral
motion is due to mean velocity components present in a plane
normal to the duct axis, typically only a few percent of the local
axial mean velocity. The secondary flow velocities arise from an
axial vorticity component generated by gradients of the Reynolds
stresses in the axial plane, a generation mechanism present in all
ducts not possessing a rotational axis of symmetry.

The square duct is perhaps the most extensively studied experimen-
tal geometry /1,2,3/, with each corner of the square duct having a
symmetrically located pair of counter-rotating secondary flow
cells. A study has also been made of the mean velocity and
Reynolds stress distribution in an equilateral triangular duct
/4/, which showed a similar distribution to the square duct. Pairs
of counter-rotating secondary flow cells were present in the duct
corners. The equilateral triangle is an approximation to the
geometry formed by a triangular rod array spaced at unity p/d
ratio, and the maximum secondary flow velocities found by /4/
were 1.5 % of the local mean axial velocity.

Such levels of secondary flow, if present within the subchannels
formed by the flow areas between rods in rod bundle arrays, would
have considerable significance in both the turbulent momentum and
heat transport processes. The results of turbulent mixing experi-
ments in rod arrays, in which /5/ is typical, have shown that the
mass diffusion rate through the rod gap region is insensitive to
the gap width for an extended range of p/d ratios and Reynolds num-
bers. This result suggests the presence of large scale turbulent
transport process within the subchannel, since for a simple
gradient driven diffusion process, the intersubchannel mass trans-
fer rate would be directly proportional to the rod gap width.

The direct measurement of secondary flow velocity components for rod bundle flow has proved to be experimentally inconclusive. Kjellström /6/ used a triangular lattice of rods spaced at a p/d ratio of 1.217, measuring the mean flow parameters and five Reynolds stress components. Although secondary flow measurements were reported, they were not symmetrical and indicated a circulation around one rod of the array: the effect was attributed to either entry conditions or array constructional tolerances. Trupp and Azad /7/ in a similar study used a triangular array spaced at three p/d ratios, 1.50, 1.35 and 1.20, and inferred secondary flow cells, transporting higher momentum fluid to the rod gap from the subchannel centre, from the turbulent kinetic energy distribution and wall shear stress variation. No direct measurements were reported, however, of secondary flow velocities. Rowe /8/ used a laser Doppler anemometer with water as the working fluid to study the mean velocity distribution and two Reynolds stress components for a square pitch array spaced at two p/d ratios, 1.250 and 1.125. Multiple secondary flow cells were suggested for the repeated symmetry area of the subchannel, deduced from the axial turbulence intensity distribution. Secondary flow velocities were not directly resolved. A study by Carajilescov and Todreas /9/ for a triangular array spaced at a p/d ratio of 1.123, using a laser Doppler anemometer and water as the working fluid, again failed to directly resolve secondary flow cells.

The numerical modelling of developed turbulent flow through rod bundle arrays has, however, focussed largely on the prediction of an axial vorticity component or secondary flow cells in the repeated symmetrical areas of the array. Carajlescov and Todreas /9/ used a one equation model of turbulence, linking the turbulent kinetic energy to the Reynolds shear stresses in the axial momentum equation. The numerical model was based on Launder and Ying's /10/ solution of developed single phase flow in a square

duct, and assumes that gradients of the normal components of the Reynolds stresses in an axial plane are the significant terms for the production of axial vorticity. Two secondary flow cells, for the repeated symmetry zone of a triangular array spaced at a p/d ratio of 1.123, were predicted. Trupp and Aly /11/ used a similar one equation model of turbulence, based on /10/, in a triangular array spaced for one study at a p/d ratio of 1.123. The Reynolds shear stress component $-\rho\overline{vw}$ as well as the normal Reynolds stress components $-\rho\overline{v^2}$, $-\rho\overline{w^2}$, were used in the production term of the axial vorticity. One basic secondary flow cell was predicted for each of the repeated flow symmetry areas. The secondary flow components V and W were predicted to become a larger percentage of the local axial velocity U with increasing Reynolds number, reaching a maximum of 2 % of U for a p/d ratio of 1.123 and Reynolds number of 200 x 10^3. The effect of an anisotropic eddy diffusivity was also examined numerically, and found to greatly reduce the wall shear stress variation as well as the level of secondary flow velocities.

Benodekar and Date /12/ used a two equation model of turbulence, involving the turbulent kinetic energy and dissipation rate, to obtain predictions of the mean axial velocity distribution in a triangular pitch seven rod cluster enclosed by a cylindrical duct. The Reynolds stresses were linked to an algebraic function of the turbulent kinetic energy and dissipation rate, rather than the length scale used by /9/ and /11/. The maximum level of the secondary flow velocities for an interior subchannel was 0.5 % of U for a p/d ratio of 1.250, and was obtained by using a combination of the adjustable model constants which also gave reasonable agreement with experimental rod bundle friction factor data. The secondary flow velocities were predicted to be considerably higher in the outer subchannels near the circular duct wall, reaching 3.5 % of the local axial velocity. At this level the secondary flow cells should be readily detected by either a laser Doppler anemometer, or by a rotated inclined wire probe and hot-wire anemometry.

A distributed parameter experiment was made by Seale /13/, model-
ling the heat transfer process in the rod gap area. The test
section, a retangular duct, contained four rods spaced at the
three p/d ratios of 1.833, 1.375 and 1.10. The heat transfer was
not from the rod surface to the air coolant, but from a heated top
wall of the duct to a water cooled lower wall. The insulated rod
walls were estimated to contribute, by conduction, to only about
2 % of the total heat flow. The remainder was transported by turbu-
lent transport and diffusion processes through the rod gap. It was
found that the eddy heat diffusivity in the rod gap region was
strongly anisotropic, with little evidence of secondary flow.

In summary, secondary flow cells have been shown experimentally to
be present for developed single phase turbulent flow through an
equilateral triangular duct, a geometry closely approximating a
triangular rod array spaced at unity p/d ratio. Direct experimen-
tal measurement of an axial vorticity component for parallel flow
through open rod array has, however, not yet been reported. An
additional flow mechanism, creating the anisotropic eddy
diffusivity of heat measured by /13/ for the rod gap area, may
therefore be present as the dominant process for in-line flow
through open rod arrays.

2. Experimental Rigs

The experimental data of the mean axial velocity distribution,
wall shear stress variation and Reynolds stress distribution for
developed single phase flow through two rod bundle geometries is
referred to in this report. The first test section is rectangular
in cross-section and contains four highly polished rods spaced at
five pitch to diameter (p/d) and wall to diameter (w/d) ratios.

The second test section, constructed from six highly polished rods set in a square pitch, represents the flow area typical of the interior regions of a large square pitched rod array.

2.1 Wall bounded rod array

The rectangular duct containing the wall bounded rod array is shown by fig. 1, spaced at one of the p/d and w/d ratios used in the series. The complete measurement data of the experiments is contained in references /14 - 23/, with only part of these studies reproduced for reasons of space. The aluminium tubes were machined to a high surface finish, with a mean roughness depth of the surface of only 0.6 m. The rectangular channel was manufactured from plexiglass, with one of the end or short walls being adjustable to allow the channel geometries to be changed. The overall length of the test section was 7 m, with both the rods and channel walls made up of four sections of 1.750 m length. Small pins, 2 mm diameter, were used as spacers at four levels in the test section to maintain the required array geometry. The working fluid was air, delivered to the test-section through an open honeycomb filter. The air supply system, powered by a radial blower, had an air filter unit of 1 μm particle size to avoid contamination of the hot wire elements.

The diameter of the rods for the rig shown by fig. 1, is 157.5 mm. For this typical duct arrangement , the rods were placed assy-metrically inside the rectangular channel. The wide rod to wall gap is 18.60 mm, giving a w/d ratio of 1.118, and the narrow gap 4.10 mm for a respective w/d ratio of 1.026.

The ratio of the tube diameter in the test-section to a typical fuel pin diameter for a nuclear power reactor is 12.5 : 1. However, as the important scaling number for a single phase

turbulent reactor coolant is the Reynolds number, the velocity field in the test-section preserves dynamic similarity.

Measurements were made of:

(a) the mean axial fluid velocity (Pitot tube).
(b) the turbulent shear stresses in the radial and circumferential directions (hot-wire anemometer).
(c) the distribution of turbulence intensities and the turbulent kinetic energy (hot-wire anemometer).
(d) the distribution of the wall shear stress (Preston tube, using the correlations of Patel /24/).

The data from the studies /14 - 23/ are arranged in Section 4 to demonstrate the effect of changing the test section geometry in two general methods.

   (i) Constant p/d and variable w/d
   (ii) Variable p/d ratio with p/d = w/d (symmetric w/d)

For the first case five experimental investigations were performed. For p/d = 1.071 the following wall-to-diameter ratios were tested:
- 1.026   /15/
- 1.048   /18/
- 1.071   /21/
- 1.096   /19/
- 1.118   /14/

Test sections with p/d = w/d were tested in the second study for:

- P/D = 1.071   /21/
- P/D = 1.15   /22/
- P/D = 1.4   /23/

The study for a p/d = 1.036, w/d = 1.071 /20/ is included in the second analysis, as it was considered that the effect of the larger rod to wall gap should not propagate significantly into the rod to rod gap area ($\theta \leq 35°$). The data are compared along the experimentally determined line of maximum velocity (or M.V.L.) in the wall subchannel. All Reynolds stress data is normalised by the local wall shear stress.

2.2 Symmetrical square pitch rod cluster

The six rod cluster forming a symmetrical test section, fig. 2, is intended to model the fluid mechanics in the interior of a large square-pitch rod array. Although data was taken for all rods of the array /25/, the area between 0 and $\pm$ 45° and the centreline of the duct for the top and lower central rods of the array is considered to most closely model the repeated symmetry area of a large rod array. A numerical solution of the axial momentum equation for both laminar and turbulent developed flow /26/, showed the presence of the walls in the outer rod gaps to have a decreasing effect on the mean velocity solution in the centre of the subchannel as the p/d ratio was reduced. The laminar flow solution, for a p/d ratio of 1.107, showed the effect of the rod gap walls to penetrate a neglegible distance into the central area of each subchannel /26/.

The rod diameter was 140 mm, and the test section length 9.14 m. The axial pressure gradient was determined by 19 static tap stations, spaced equally at 457 mm intervals along the test section. The ratio of the test section length to hydraulic diameter is 128. This was considered to be sufficient to ensure developed flow conditions at the normal measurement plane, located in an axial plane 100 mm before the test section exit.

Air is the working fluid, and the same measurements as detailed in section 2.1 were made of the developed single phase turbulent flow. All components of the Reynolds stresses, including the $-\rho\overline{vw}$ component, were measured by a rotated two element hot wire anemometer probe. The independence of the mean flow and Reynolds stress distribution to the rig entry conditions was established experimentally /25, 27/. This was shown by changing from a sharp edged entry with flow separation and reattachment, to a fine mesh filter screen at the test section entry sufficient to create a pressure loss approximately equal to the whole test section length. No measurable difference in any parameters was found for the two cases, showing the flow to be developed. The hot-wire probe geometrical, constructional, and calibration details are presented in /25/. A computer was used on-line to position the probe in three axes, measure the required basic data and to perform a statistical analysis to ensure a preset accuracy limit had been reached /25/. All data reduction was performed by the same computer, which also monitored the long term drift of the hot wire anemometer probes, due to either wire resistance drift or changes in the ambient temperature and pressure.

The Reynolds number dependence of the mean velocity distribution, wall shear stress variation and Reynolds stress distribution was tested over a 9 : 1 Reynolds number range /28/, covering the range 22.6×10^3 to 207.6×10^3. Weak Reynolds number dependence was shown for some of the parameters: however, for reasons of space only part of one study is included in this report.

3. Equations of motion and boundary conditions

3.1 Momentum Equations

The continuity equation, and the fluid momentum or Navier-Stokes equations for a constant viscosity and density fluid in polar co-ordinates are (Hinze /29/):

Continuity:

$$\frac{\partial U}{\partial z} + \frac{1}{r} \frac{\partial (rV)}{\partial r} + \frac{1}{r} \frac{\partial W}{\partial \theta} = 0 \tag{1}$$

z axis momentum:

$$\rho \frac{DU}{Dt} = - \frac{\partial p}{\partial z} + \mu \nabla^2 U - \rho \frac{\partial \overline{u^2}}{\partial z} - \frac{\rho}{r} \frac{\partial (r\overline{uv})}{\partial r} - \frac{\rho}{r} \frac{\partial \overline{uw}}{\partial \theta} \tag{2}$$

r axis momentum:

$$\rho \left(\frac{DV}{Dt} - \frac{w^2}{r}\right) = - \frac{\partial P}{\partial r} + \mu \left(\nabla^2 v - \frac{v}{r^2} - \frac{2}{r^2} \frac{\partial w}{\partial \theta}\right) - \frac{\rho}{r} \frac{\partial (r \overline{v^2})}{\partial r}$$

$$- \frac{\rho}{r} \frac{\partial \overline{vw}}{\partial \theta} - \rho \frac{\partial \overline{uv}}{\partial z} + \rho \frac{\overline{w^2}}{r} \tag{3}$$

θ axis momentum:

$$\rho \left(\frac{DW}{Dt} + \frac{VW}{r}\right) = - \frac{1}{r} \frac{\partial P}{\partial \theta} + \mu \left(\nabla^2 w - \frac{w}{r^2} + \frac{2}{r^2} \frac{\partial V}{\partial \theta}\right)$$

$$- \frac{\rho}{r} \frac{\partial \overline{w^2}}{\partial \theta} - \rho \frac{\partial \overline{vw}}{\partial r} - \rho \frac{\partial \overline{uw}}{\partial z} - 2\rho \frac{\overline{vw}}{r} \tag{4}$$

The ∇^2 operator represents

$$\frac{\partial}{\partial z^2} + \frac{\partial^2}{\partial r^2} + \frac{1}{r} \frac{\partial}{\partial r} + \frac{1}{r^2} \frac{\partial^2}{\partial \theta^2}$$

and the fluid total derivative

$$\frac{D}{Dt} = \frac{\partial}{\partial t} + \frac{U\partial}{\partial z} + \frac{V\partial}{\partial r} + \frac{w}{r}\frac{\partial}{\partial \theta}$$

The rig axial direction is along the z axis. For the interior region of a large symmetrical rod array set in a regular square lattice, a symmetrical low zone between the rod wall, at O and 45° and the subchannel centre line may be abstracted as the repeated symmetry area of the array. This area is shown by fig. 3 as bounded by the rod wall AD, radial lines AC and CD and the sub-channel centre line BC. The six rod cluster test section (Section 2.2) is an approximation to a large array. However, the flow area bounded by the top and subchannel diagonals at $\pm$ 45° was shown, by a laminar flow solution to the axial momentum equation, to closely represent the equivalent infinite rod array for p/d ratios equal to or less than 1.20 /26/.

The static pressure field for developed flow conditions is

$$P(z,r,\theta) = c_1 z + \Phi (r,\theta) \tag{5}$$

where c_1 is the constant axial pressure gradient. For developed flow conditions, all axial derivatives of both the mean and turbulent velocity components are zero.

The wall no-slip velocity condition means that U, V and W are zero along the rod wall, AD. Symmetry applied to the area ABCD implies that the secondary flow components V and W cannot cross the cell boundaries. Thus W is zero for radial traverses at θ = O and 45°, although V is only required to be zero at the subchannel centre B or rod gap centre C. The symmetric functions across the reflection boundaries AB (θ = 45°) and CD(θ = 0°) are P, U, V, $-\overline{\rho u^2}$, $-\overline{\rho v^2}$, $-\overline{\rho w^2}$, $-\overline{\rho uv}$. Antisymmetry across the same reflection boundaries,

meaning a change in sign but not magnitude, applies to W, $-\rho\overline{uw}$ and $-\rho\overline{vw}$. The Reynolds shear stresses $-\rho\overline{uw}$, $-\rho\overline{vw}$ are also zero for the $\theta = 0$ and 45° reflection boundaries although, as noted by Trupp and Aly /11/ the azimuthal derivatives $(\frac{1}{r}\frac{\partial}{\partial\theta})$ are not necessarily zero.

For no nett azimuthal transfer of momentum across boundaries AB and CD, the azimuthal momentum equation (4) vanishes, implying

$$\frac{1}{r}\frac{W}{r}, \quad \frac{\partial^2 W}{\partial r^2}, \quad \frac{1}{r^2}\frac{\partial^2 W}{\partial\theta^2} \quad \text{and} \quad \frac{1}{r}\frac{\partial V}{\partial\theta}, \quad \frac{1}{r}\frac{\partial\Phi}{\partial\theta}$$

are all zero. the Reynolds stress terms $\frac{-\rho}{r}\frac{\partial\overline{w^2}}{\partial\theta}$, $-\rho\frac{\partial\overline{vw}}{\partial r}$

are also zero. No comparable simplifications appear to be possible for the axial and radial momentum equations. A discussion of the associated turbulent kinetic energy equation for a square pitch rod array is presented by Wood /30/.

3.2 Axial vorticity equation

The analysis of Perkins /31/ of the formation of a streamwise vorticity in turbulent flow shows the terms thought to be associated with the generation of the axial vorticity. The axial vorticity equation may be derived by using the curl operator with the θ and r axis momentum equations (3) and (4).

For the steady state flow case, the axial vorticity Ω_z is given by:

$$\rho \, \frac{D\Omega_z}{Dt} \;=\; \rho \left(\frac{U \partial \Omega_z}{\partial z} + \frac{v \partial \Omega_z}{\partial r} + \frac{W}{r} \frac{\partial \Omega_z}{\partial \theta} \right),$$

$$= \mu \nabla^2 \Omega_z + \Omega_z \frac{\partial U}{\partial z} + \underbrace{\frac{\Omega_r}{r} \frac{\partial (rU)}{\partial r} + \frac{\Omega_\theta}{r} \frac{\partial U}{\partial \theta}}_{P_1} - \underbrace{\frac{\rho}{r^2} \frac{\partial^2 (r (\overline{w^2} - \overline{v^2}))}{\partial r \partial \theta}}_{P_2}$$

$$- \underbrace{\frac{\rho}{r} \left(\frac{\partial}{\partial r} \left(\frac{r\partial}{\partial r} \right) + \frac{2\partial}{\partial r} - \frac{1}{r} \frac{\partial^2}{\partial \theta^2} \right) \overline{vw}}_{P_3} - \underbrace{\frac{\rho}{r} \left(\frac{\partial^2 (r \, \overline{uw})}{\partial r \partial z} - \frac{\partial^2 \, \overline{uv}}{\partial \theta \partial z} \right)}_{P_4}$$

$$(6)$$

The vorticity components are:

$$\Omega_z = \frac{1}{r} \frac{\partial (rW)}{\partial r} - \frac{1}{r} \frac{\partial v}{\partial \theta}$$

$$\Omega_r = \frac{1}{r} \frac{\partial U}{\partial \theta} - \frac{\partial W}{\partial z} \qquad (7)$$

$$\Omega_\theta = \frac{\partial V}{\partial z} - \frac{1}{r} \frac{\partial (rU)}{\partial r}$$

The total derivative of the axial vorticity is considered to be a convective transport term, and not associated with the production of axial vorticity. The viscous term is not connected with the production of the vorticity but rather with viscous dissipation. The component $\Omega_z \frac{\partial U}{\partial z}$ is associated with the axial stretching of vorticity. The terms linked to the production of the axial vorticity are labelled P_1 to P_4, after Perkins /31/.

The term P_1 is responsible for the production of secondary flows
of the first kind, by turning or skewing the axial flow. The
development of a transverse velocity component for a fluid flowing
in a curved duct was noticed initially in winding river beds. The
mechanism of turning or skewing an axial flow to generate an axial
vorticity applies equally to skewed turbulent boundary layer or
closed duct flow.

Expansion of the P_1 term to

$$(\frac{1}{r} \frac{\partial U}{\partial \theta} - \frac{\partial w}{\partial z}) \cdot \frac{1}{r} \frac{\partial rU}{\partial r} + (\frac{\partial V}{\partial z} - \frac{1}{r} \frac{\partial rU}{\partial r}) \frac{1}{r} \frac{\partial U}{\partial \theta}$$

shows, for developed axial flow in the z direction with zero axial
derivatives, the term to be zero. It is apparent that for flow in
a closed duct, flow skewing induced by the duct entry may persist
in the form of an axial vorticity for a long axial distance. The
independence of the flow structure from the rig entry conditions
may therefore be a sufficient experimental test to eliminate the
possibility of secondary flow effects due to flow skewing.

Secondary flows of the second kind are a turbulence induced
effect, and originate in non-zero local values of the production
terms P_2 to P_4, which may be better viewed as redistribution terms
as the integral over the duct is zero. The terms represent the sum
effect of the time averaged convection and production of the
turbulent vorticity. For developed flow conditions, P_4 is zero
because of the axial derivative term.

4. Experimental Results

4.1 Wall bounded rod array

The experimental results of the wall shear stress variation and turbulence intensity distribution in the wall bounded rod array (fig. 1), have been summarized to demonstrate the effects of geometry on the developed turbulent flow field /32/. The complete experimental data for these experiments is contained by references /14 - 23/.

4.1.1 Wall shear stress variation
_____

The experimental wall shear stress variation for a w/d ratio of 1.118 is shown by fig. 4, together with a numerically predicted wall shear stress variation computed by the VELASCO code /33/. The rod centered data, measured in polar cylindrical co-ordinates, is referenced to a zero angle of θ in the centre of the rod to rod gap. The retangular duct wall shear stress variation, measured in a cartesian co-ordinate system, is centered on an axis origin located on the rod wall and in the centre of the rod to wall gap. For the case of a wide gap the agreement between computed and measured data is fair, especially for the channel wall. The maximum difference is found for the gap between the rods (11.2 %). The agreement is bad for w/d = 1.026. Here the maximum difference is 38 %, and is for the gap between rod and channel wall (fig. 5).

The reason for this discrepancy is clear: VELASCO does not model the high turbulence intensities in narrow gaps. The momentum transport in circumferential direction is calculated by aniso-tropic eddy viscosities and by an assumed secondary flow cell by VELASCO. However, the anisotropy assumed in VELASCO is very small in comparison with the experimental data.

The same problem in predicting the wall shear stress variation for the narrow gap between the rod and channel walls is true for the narrow gaps between rods (fig. 6). In this case the maximum deviation between the experimental data and the VELASCO prediction is 31 % in the gap between the rods, for a p/d ratio of 1.036.

The effect of changing a w/d ratio, or the wall gap width, while maintaining a fixed rod p/d ratio on the rod wall shear stress variation is shown by fig. 7. The p/d ratio is 1.071, and five w/d ratios, 1.026, 1.048, 1.071, 1.096, 1.118 are shown. A clear and systematic trend is evident from the experimental data. As the rod to wall gap is reduced, the minimum shear stress in this region (θ = 90°) systematically reduces. This is coupled to an increasing level of shear stress in the rod to rod gap (θ = 0°). The coupling of the turbulent flow structure in these two relatively remote regions of the array, in terms of the duct hydraulic diameter, is strongly suggested by fig. 7.

The corresponding experimental duct wall shear stress variation for the same w/d ratios is shown by fig. 8. For the rod to wall gap region (x = 0 mm) the same trends are shown as for the rod wall shear stress variation (fig. 7), with little change in the shear stress distribution until the w/d ratio becomes 1.048 or lower.

The mean axial velocity distribution, for all the studies covered by the above p/d or w/d ratios, were well described by the logarithmic law of the wall distribution. The local wall shear stress was used to calculated the local wall friction velocity ($v^*(\theta)$), the parameter used to scale of the mean axial velocity ($U(r,\theta)$ and wall distance y.

4.1.2 Axial turbulence intensity

A significant finding is the very high axial turbulence intensity
near the rod to channel wall gap for a w/d ratio of 1.026
(fig. 9). For the radial traverse at 70°, fig. 9, the nondimen-
sional axial turbulence intensity $(u'(r,\theta)/v^*(\theta))$ reaches a level
of 3.6 at the line of maximum velocity (M.V.L.) near the rod gap.
The axial turbulence intensity reduces to 2.25 for the traverse
in the rod to wall gap centre, a level only reached in the near
wall region for developed pipe flow /25/.

The axial intensity distribution for the w/d ratio of 1.118 and
p/d ratio of 1.071 is shown by fig. 10. The peak level for this
region is in the rod to rod gap area, between 15 and 20°. The
axial turbulence intensity in the rod to wall gap is similar to
the radial distribution for developed pipe flow.

The signal processing used by /14 - 23/ to evaluate five of the
six Reynolds stress components used the non-linearised hot wire
anemometer bridge output, and small signal approximations to the
probe response. Caution therefore has to be exercised in the
regions where the intensity levels reach very high values, as the
approximations are certainly no longer accurate. However, it is
still possible to note the general trend of the intensity data for
the low rod to rod or wall spacing.

The axial turbulence intensity distribution in cylindrical
co-ordinates for a p/d ratio of 1.036 (w/d = 1.071) is shown by
fig. 11. In common with the study for a p/d ratio of 1.071 (fig.
10), the maximum levels are shown by the radial traverses at 15
and 20°.

The variation of the axial turbulence intensity for a fixed p/d ratio of 1.071 and variable w/d ratios between 1.026 and 1.118 is shown by fig. 12, for the M.V.L. Two different trends can be observed:

- in the region between the rods (0 - 35°) the axial intensity increases with increasing w/d in spite of the fact that the geometry remains unchanged in this region,

- in the region between the rod and the channel walls (θ = 40 - 90°) the axial itensity increases strongly with decreasing w/d. This increase is quite systematic. The absolute values for w/d = 1.026 should be considered with caution as discussed, due to the high turbulence intensity level.

A further feature is the relatively fixed location of the point of minimum axial turbulence intensity at 35°, for the M.V.L.

The data for the case p/d = w/d is shown by fig. 13. For the p/d ratio of 1.036, the w/d ratio is 1.071 and strictly this geometry is not part of the series. However, for the region between 40 and 90° the axial turbulence intensity in the rod to wall gap is shown to closely follow the data for the study with a p/d and w/d ratio of 1.071. The strong coupling between the turbulent processes in the rod to rod gap area and the rod to wall gap region, suggested by the wall shear stress distribution, is again evident in the axial turbulence intensity data.

4.1.3 Azimuthal turbulence intensity
—————————————————————————————————

The azimuthal turbulence intensity ($w'(r,\theta)/v^*(\theta)$) for a fixed p/d ratio of 1.071 and variable w/d ratios is shown by fig. 14 for the M.V.L. It is apparent that the increase in the azimuthal turbulence intensity for the rod to wall gap region as the w/d

ratio decreases is the most dominant feature of the experimental data. For w/d ratios of 1.071 or less, the azimuthal turbulence intensity at the centre of the rod gap (90°) is greater than the local axial turbulence intensity.

The same increase in azimuthal turbulence intensity, with decreasing p/d or w/d, for the centre of the rod to rod or wall gap is shown by fig. 15. The data also shows that the increase in azimuthal intensity in the rod to rod gap is slightly less than for the rod to duct wall gap for the same p/d and w/d ratio. The study for a p/d ratio of 1.036 is not in accordance with this trend, as the w/d ratio is 1.072.

The region of a local minimum in this component of the Reynolds stresses for the M.V.L. is at approximately 35°, or at the same location as the axial turbulence intensity.

4.1.4 Turbulent kinetic energy

The turbulent kinetic energy, for the fixed p/d ratio of 1.071 and variable w/d ratios, is shown by fig. 16 for the M.V.L. The very large increase in the local turbulent kinetic energy for the rod to wall gap region is seen to be balanced by a corresponding decrease in the rod to rod gap area, as the w/d ratio is reduced. It is important to remember that the turbulent kinetic energy, q, is normalized by the local friction velocity $(\frac{1}{2}(\overline{u^2}(r,\theta) + \overline{v^2}(r,\theta) + \overline{w^2}(r,\theta))/v^{*2}(\theta))$ and so only relative changes are shown by fig. 16. However, the change in turbulent kinetic energy for the rod wall gap area is considerably higher than the corresponding wall shear stress variation. Additionally, the data for a w/d ratio of 1.026 is not accurate for the rod to wall gap region, because of the high turbulence intensities in this area.

The case of p/d = w/d is shown by fig. 17, which again demon-
strates the remarkable increase in turbulent kinetic energy in the
rod gap region as the spacing is reduced.

4.2 Symmetrical square pitch rod cluster

The experimental data for the symmetrical square pitch rod cluster
(fig. 2), is presented for the central rod gap region between 10
and -20°, and for one Reynolds number of 46.3 x 10³. The p/d ratio
is 1.107. Complete experimental data for p/d ratios of 1.194 and
1.107 is given in /25, 27, 28/. The geometry of the test section
was maintained by an external frame supporting the rod bundle,
without any internal spacers or pins in the open rod gap area.

In common with the hot wire anemometry techniques used in Section
4.1, small signal approximations to the non-linearized anamometer
bridge output were used to calculated the Reynolds stresses. How-
ever, all six components of the Reynolds stresses were calculated,
and a redundant set of hot wire measurements were made to test the
accuracy of the signal approximations /25/. In all experiments the
experimental closure or self-consistency of the small signal
approximations was found to be satisfactory.

4.2.1 Wall shear stress variation

The wall shear stress variation for the top central rod of the
array is shown by fig. 18, with the centre of the open rod gap
located at 0°. The agreement of the measured wall shear stress
data points for the two Preston tube diameters is encouraging, as
the correlations used were developed by Patel /24/ in axisymme-
tric developed pipe flow. The Reynolds stress distribution for

closely spaced rod bundle flows is significantly different to the calibration duct geometry. A survey of the effect of the Preston tube diameter on the measured wall shear stress for the p/d ratio of 1.194 /25/, showed the results to be self consistent, within the limits of experimental error, for 13 tube diameters covering approximately a 9 : 1 range of diameters.

4.2.2 Mean axial velocity

The mean axial velocity distribution for angles between 10 and -20° is shown by fig. 19. Also plotted is the turbulent core region of the law of the wall logarithmic velocity profile,

$$U^+(r,\theta) = A \ln y^+ + B \tag{8}$$

with A and B coefficients of 2.388 and 5.45 as established by Patel /34/. There is a considerable range in the value of these coefficients in the literature /25, 29/. However, it is seen that the experimental velocity points are well scaled by the Patel coefficients, and the use of these values is self-consistent with the use of the same shear stress/Preston tube pressure correlation.

There is little difference between the above coefficients and the Nikuradse /34/ established values of 2.50 and 5.5 for A and B respectively. The mean axial velocity data of Section 4.1 /14 - 23/ is plotted against the Nikuradse coefficients. For all the data sets there is close agreement between the experimental points and the law of the wall distribution, showing the remarkable insensitivity of this profile to the actual turbulent flow structure in the duct.

4.2.3 Axial turbulence intensity

The axial turbulence intensity in the open rod gap is shown by
fig. 20. Also plotted is the data established for developed
axisymmetric pipe flow by Laufer /35/ and Lawn /36/. It is
apparent that the axial turbulence intensity is considerably
higher in the centre of the rod gap region than the corresponding
levels shown for developed pipe flow. This result implies either
the transport to or generation of turbulence in this region, as
turbulence is normally considered to be generated in the axial
flow direction. The same trend as shown by the wall bounded sub-
channel for the rod to rod gap region is also evident in fig. 20,
with a local minimum in the axial turbulent intensity at $0°$, and a
local maximum at approximately $-15°$.

4.2.4 Radial turbulence intensity

The radial turbulence intensity distribution is shown by fig. 21,
together with the pipe flow profiles. It is seen that in the
centre of the rod gap, the radial turbulence intensity level is
approximately equal to the pipe flow values. The studies for the
wall bounded rod bundle (Section 4.1) showed that as the p/d or
w/d ratio was reduced, the radial turbulence intensity in the rod
gap actually fell below the pipe flow values. This is physically
reasonable, as the narow rod gap region would be expected to
strongly attenuate the magnitude of velocity fluctuations normal
to the rod or duct wall. However, for the w/d ratio of 1.026 in
the wall subchannel, negative values of the radial turbulence
intensity were shown for the rod to wall gap, a physically
unrealistic prediction generated by the failure of the small
signal approximations in the highly turbulent flow.

4.2.5 Azimuthal turbulence intensity

The azimuthal turbulence intensity for the open rod gap region is
shown by fig. 22, together with the pipe flow distribution. This
component of the Reynolds stresses is seen to be considerably
above the pipe flow level, and reaches a local maximum, when
normalized by the local wall friction velocity, at the rod gap
centre (0°). It is seen, for this radial traverse, to be nearly
independent of the wall distance.

The data for the symmetrical rod cluster is also consistent with
the trends established for the wall bounded rod bundle (section
4.1) when the azimuthal turbulence intensity again becomes a
maximum at the centre of the rod-to-rod or wall gap. This result
suggests the existence of a strong turbulent transport process
into the rod gap area. However, as the data contained by /25, 27,
28/ shows, no non-zero secondary flow velocity components V or W
were detected in the flow area between 0 and 45° about the central
rods of the array and the duct centre-line. The accuracy of direct
measurement, as estimated by /25/, is approximately 1 % of the
local axial mean velocity.

4.2.6 Radial Reynolds shear stress

The radial component of the Reynolds shear stress normalized by
the local friction velocity is shown by fig. 23. At the centre of
the rod gap (0°), the distribution is seen to be almost linear.
For this radial traverse it is also zero at the gap centre-line,
as required by symmetry, and asymptotes to the local wall shear
stress. Away from this line of symmetry, the radial Reynolds shear
stress distribution departs markedly from the linear radial
distribution.

4.2.7 Azimuthal Reynolds shear stress

The azimuthal component of the Reynolds shear stress is an
antisymmetric function with respect to symmetry boundaries. The
experimental results about the radial traverse at 0° show this
feature, with approximately the zero level required by symme-
try. This component of the Reynolds stresses increases in a
remarkable manner away from the rod gap centre, being approxi-
mately $1.3\,\tau(\theta)$ for the traverse at -15° and the duct centre line.
The absolute level is weakly dependent on the Reynolds number,
being 1.2 for a Reynolds number of 22.6×10^3, and 1.6 for a
Reynolds number of 207.6×10^3 /28/. The location of the maximum
value of the azimuthal Reynolds shear stress is, however, constant
at 15°. The very high levels of the azimuthal Reynolds shear
stress, which increase in magnitude as the p/d or w/d ratio is
reduced, is also a feature of the wall bounded rod bundle studies
(Section 4.1).

4.2.8 Planar Reynolds shear stress

The Reynolds shear stress formed by the product of the two tur-
bulent velocity components normal to the duct axis and normalized
by the local wall shear stress, is shown by fig. 25. The component
is difficult to measure accurately by a rotated inclined hot wire
probe, being essentially the difference of two large quantities
/25/. However, the non-zero values of this Reynolds stress
component for the rod gap area, and the antisymmetric behaviour
across the radial traverse at 0°, is shown by fig. 25. The
non-zero values of the planar Reynolds shear stress were only
present for the p/d ratio of 1.107 and traverses between $\pm 35^\circ$
about the central rods of the array. For the study at a p/d ratio
of 1.194, the planar Reynolds shear stress was effectively zero
for the whole duct /25/.

4.3 Auto and cross-correlation functions in the wall bounded rod array

In order to resolve the possible flow mechanism generating the high axial and azimuthal turbulence intensities in the rod gap region, as shown by the studies of Sections 4.1 and 4.2, a study was made of the flow structure in the wall bounded rod array for a p/d ratio of 1.036 /37/. The w/d ratio was 1.072 for both walls bounding the central rods of the duct, and thus the radial traverse at 0° is a true symmetry boundary for the test section. A cartesian co-ordinate system, centered in the rod gap centre was used in this study (fig. 26), rather than the rod centered polar co-ordinate system used by the experiments of Section 4.1 and 4.2. 10^4, which is equal to /20/. A constant Reynolds number was maintained by reference to a scaled pressure measured by a fixed pitot probe located in one corner of the rectangular duct. The flow rate was corrected for air temperature and density changes.

Two hot wire probes were used to establish the auto and cross-correlation functions reported. Both probes consisted of a single normal wire and a single inclined wire element, with the inclined wire element located centrally on the probe axis. The sensor element was 2 mm long 5 m diameter tungsten wire, and the probe manufacturing and calibration techniques are described in /25/.

The non-linearised bridge output signals from DISA constant temperature hot wire anemometer bridges were high pass filtered at 0.1 Hz, and directly recorded by F.M. tape modules on an E.M.I. 7000 series tape recorder. Two methods of processing the tape recorded turbulence signals were used. The first used a direct analog network solution of the small signal approximations to the wire equations /8/, and analog multiplication and integration of the appropriate turbulence components, to obtain the required auto and cross-correlaion coefficients. Although relatively fast signal processing is possible, only the zero time lag point of the functions are calculated.

The second method involved the use of a small computer to digitalize the tape signals, after the use of an anti-aliasing low pass filter set at 732 Hz. The digitalizing rate was 2048 Hz, and record lengths of 100 seconds were made for processing on a large IBM computer. The small signal approximations to the wire equations were used to compute the time record of the relevant turbulent velocity component, which was then used to generate auto and cross-correlation functions.

4.3.1 Direct reproduction of turbulent velocity components
_____

The turbulent velocity components for two points in the rod gap, point 2 located at (x,y) co-ordinates (0, -10 mm) and point 4 at (0,10 mm) are shown by fig. 27a and b. The time record length of 0.1 seconds is far less than the time used in computing the correlation functions. However, there is clearly shown to be a considerable large scale structure in the axial velocity fluctuations at both locations for the x-z plane (fig. 27a). The mean axial velocity U at these locations was 20.5 ms^{-1}, and the peak excursion of the axial turbulence component u is approximately 25 % of this value. This result indicates that the small signal approximations to the anemometer bridge output are not accurate. However, the signals are sufficient to show the possibility of a correlation between the axial velocity fluctuations on either side of the rod gap symmetry line or x axis.

The turbulence component along the x axis, v, is seen to be considerably reduced in magnitude, with little evidence of the large scale structure of the axial component. The v signal is more typical of the non-axial turbulent velocity components in developed internal duct flows at high Reynolds numbers. The lack of a large scale structure and reduced intensity for v in the rod gap is not surprising, as the narrow gap width must dampen and restrict velocity fluctuations normal to the rod surface.

The velocity component along the y axis, w, is seen in fig. 27b to have an almost periodic large scale structure. The magnitude of the velocity fluctuations in w is at least equivalent to the axial velocity fluctuation at both locations. There is more fine scale turbulence superimposed on the transverse or w component than u. The plotting system used to generate the record was estimated to be capable of resolving frequency components to 2 kHz, after allowing for the maximum tape speed down ratio of 64 : 1. The large scale structure of w is clearly correlated across the rod gap centre-line. The presence of a large scale, energetic and periodic momentum exchange process through the rod gap is strongly suggested by fig. 27b.

4.3.2 Cross-correlation coefficients within one subchannel

In order to resolve the extent of penetration of the large scale structure present in the rod gap into the subchannel, the cross-correlation coefficients between the same velocity components were measured along the subchannel centre line or y axis. A fixed hot wire probe 1 was located at (x,y) coordinates of (0,10 mm) and probe 2 moved along the y axis between this location and (0,55 mm). The analog signal processing system was used to generate the results shown by fig. 28, and so all the higher frequency components of turbulence, which are unlikely to correlate over large distances, contributed to the individual signal variances. This effect would reduce the magnitude of the correlation coefficients generated by the large scale structure.

The axial velocity component u is seen to be significantly correlated for a considerable distance from the rod gap area. The furthest data point, corresponding to a y_2 value of 55 mm, is in the same region of the subchannel reached by a radial traverse at 35°. The results of /20/ show a significant reduction in the axial turbulence intensity for this region, after the elevated levels nearer the rod gap.

The transverse turbulent velocity component w, directed towards the rod gap, is also well correlated over the same distance. The cyclic intersubchannel momentum exchange process apparently extends over a considerable extent of the subchannel.

The x axis or v component of the turbulence is seen to have no significant correlation for the whole traverse length. This result appears feasible in view of the absence of a large scale structure in this component, as shown by fig. 27a.

4.3.3 Auto-correlation functions
_____

The auto-correlations of the axial and transverse turbulent velocity components were computed for the rod gap region at locations 1 to 4, shown in Table 1.

Probe Location No.	X_{mm}	Y_{mm}
1	0.	0.
2	0.	-10.
3	0.	5.
4	0.	10.

Probe locations for auto and cross correlation functions
Table 1

One hot wire probe was fixed at co-ordinate location 2, and the moving probe at the other tabulated locations. The digital analysis method outlined by section 4.3 was used, and so turbulence components with a frequency higher than the antialiasing filter set at 736 Hz were removed before processing.

The axial velocity component u shows little evidence of a periodic function for the rod gap centre, as shown by fig. 29a. However, away from the x axis symmetry line, the axial component of

turbulence does show a damped periodic responce, with a cyclic
frequency of 92 Hz (fig. 29b,c,d). This frequency is repeated in
all the periodic auto and cross correlation functions measured,
and represents an average frequency of the cyclic momentum inter-
change process for the 100 second time records used in the compu-
tation. The correlation functions were computed for a 0.25 second
record length and were ensembled averaged over 400 functions.
However, only the first 50 milliseconds of the functions show
significant values.

Rowe /8/ in a square pitched rod array using water as the model-
ling fluid and a laser Doppler anemometer to measure the mean and
turbulent velocity components, noted a periodic behaviour in the
auto-correlation functions for the axial turbulent velocity compo-
nent. This periodic behaviour was only present in the rod gap
region and only for the lower p/d ratio used of 1.125.

The transverse turbulent velocity component w shows a periodic
auto-correlation at all locations, fig. 30a,b,c and d, with strong
evidence of the 92 Hz component.

4.3.4 Spatial Correlations

The spatial correlation function between the axial turbulent velo-
city fluctuations at locations 1 and 2, fig. 31a, shows a relati-
vely high correlation with little evidence of the dominant perio-
dic fluctuation. However, the corresponding correlation function,
fig. 31b, for the locations equidistant across the rod gap sym-
metry or x axis does show evidence of this periodic component,
although at a reduced magnitude. A phase shift of approximately
45° for the periodic part of the signal is also indicated.

The transverse or w turbulent velocity cross correlation for both
locations, fig. 31c,d, strongly shows the high spatial correla-
tion for the periodic component across the rod gap. There is
little evidence of a phase shift (fig. 31d), however, between
locations 2 and 4 on opposite sides of the x axis, for this compo-
nent of turbulence.

4.3.5 Reynolds shear stress

It has been demonstrated experimentally /25, 27, 28/ that this
component is antisymmetric with respect to the x axis or symmetry
boundary in the rod gap. An examination of the cross-correlation
function for these turbulent velocity components at the rod gap
centre, fig. 32a, and at locations 2 and 4 on either side of the x
axis, fig. 32b, c, shows the high magnitude of this Reynolds
stress component to be associated with the cyclic fluctuation
centered at 92 Hz. Although it is difficult to talk of the phase
of a signal that is jittering in both amplitude and frequency as
is shown by fig. 27b, fig. 32a,b and c suggest that the change of
sign of -   is connected to a phase shift between u and w. There
is approximately a 90° phase shift between these components at the
rod gap centre or location 1, generating the required zero value.
For location 2, fig. 32b, the phase shift is 180° changing the
sign of this Reynolds stress component with respect to location 4
(fig. 32c) which has no apparent phase shift.

The multiplication process implicit in the auto and cross-corre-
lation functions is a non-linear operation, and it is not possible
to compare these apparent phase shifts with values obtained for
the other velocity components. However, these functions were calcu-
lated for sufficiently long record lengths to give reasonable
statistical accuracy, and without recourse to any of the condi-
tional sampling techniques used in many structual studies of
turbulence.

4.3.6 Spectra of turbulent velocity components u and w

The power spectra of the axial and transverse turbulent velocity
components at location 4 is shown by fig. 33 a and b. The axial
turbulent velocity spectra shows a local peak around 90 Hz, and
part of the spectra approximates to the -5/3 power law. However
the transverse turbulent velocity component is seen to have little
evidence of a -5/3 region, with a very large peak centered around
90 Hz.

The very strong cyclic component of w, demonstrated by the auto-
correlation studies, is confirmed by the power spectra curve
(fig. 33b). The anti-aliasing filter for the digital analysis of
these spectra was set at 2000 Hz, with a digitization rate of
4000 Hz.

5. Discussion

5.1 General summary

The experimental results contained in setion 4 and the associated
reports may be summarized under the following points:

(i) All mean axial velocity data, scaled by the appropriate local
    wall friction velocity, is in close agreement for the turbu-
    lent core region with the logarithmic law of the wall.

(ii) The axial turbulence intensity in rod to rod or rod to wall
     gaps increases with decreasing p/d or w/d ratrio. The maximum
     axial turbulence intensity is in the region of 15 to 20°, not
     the gap centre, for a rod centered cylindrical co-ordinate
     system. This trend continues to the minimum w/d ratio studied
     of 1.026.

(iii) The azimuthal turbulence intensity in the rod to rod or wall
gap region increases with decreasing p/d or w/d ratio.
Unlike the axial turbulence intensity, this component of the
Reynolds stresses reaches a local maximum in the centre of
the gap ($0°$), when scaled by the local friction velocity.
For p/d ratios equal to or less than 1.036, and w/d ratios
less 1.071, the azimuthal turbulence intensity in the rod
gap area becomes greater than the axial turbulence inten-
sity.

(iv) There was, for the rod gap region, no significant directly
measured non-zero secondary flow velocity components V and W
measured in any of the studies. The estimated resolution
limit of the rotated inclined hot wire probe is of the order
of 1 % of the local mean axial velocity.

(v) The wall shear stress variation, axial and azimuthal turbu-
lence intensity distribution, and the distribution of turbu-
lent kinetic energy for the wall bounded rod array, show
clearly that the turbulent flow structure in the rod to rod
gap and in the wall to rod gap region is closely coupled.

(vi) The azimuthal Reynolds shear stress, although zero along
lines of symmetry, reaches very high levels in the rod gap
area for close p/d ratio arrays. The same effect is present
in closely spaced rod to wall geometries, or for low w/d
ratios.

(vii) The planar component of the Reynolds shear stress, $-\rho\overline{vw}$,
becomes of significant magnitude for the open rod gap region
for a p/d ratio of 1.10. This component reaches a maximum
between 15 and $20°$, becoming zero for radial traverses at
angles greater than approximately $35°$.

(viii) The high level of azimuthal and axial turbulence intensity, for rod gap region in the wall bounded rod array at a p/d ratio of 1.036, was shown to be associated with a large scale, highly energetic turbulent velocity fluctuation.

(xi) The azimuthal turbulent velocity component, w, was shown to have in the rod gap area for the p/d ratio of 1.036, an almost periodic large scale structure. This component was highly correlated across the rod to rod centre line (or x axis in fig. 26), a symmetry line that secondary flow cells would not cross in a symmetrical array.

(x) For the same rod gap region in the wall bounded rod array (p/d = 1.036), there was no evidence of a large scale structure in the turbulent velocity component v normal to the rod wall.

It therefore appears that secondary flow components play little, if any, part in the highly energetic momentum exchange processes that are present in the gap region of closely spaced rod arrays. A further indication of the possible magnitude of the secondary velocity components V and W may be obtained by consideration of the axial momentum balance for the symmetrical four rod array. This balance is developed from the axial momentum equation in a manner suggested by Wood /30/. Trupp and Azad /7/ developed the same balance equation without evaluating the contribution of the azimuthal Reynolds shear stress component.

5.2 Axial momentum balance

The integration of the axial momentum equation,

$$
\rho \int_{R}^{R+y} r \left(V \frac{\partial U}{\partial r} + \frac{W}{r} \frac{\partial U}{\partial r} \right) dr = - \frac{\partial P}{\partial z} \cdot \left(\frac{y^2 + 2Ry}{2} \right) - R \, \tau_w(\theta)
$$

$$
- \rho \overline{uv} \cdot (y + R) - \rho \int_{R}^{R+y} \frac{\partial \, \overline{uw}}{\partial \theta} dr
$$

(9)

using the numerical technique developed by /25/, is detailed by Appendix A. The advection term of equation 9, containing the possible secondary flow velocites V and W, is the unknown or balance term in this equation. If V and W are both zero for the radial integration at the given angle, the R.H.S. terms of the equation should, within experimental limits, generate a zero balance level at each point of the traverse. The results of the axial momentum balance applied to radial traverses angles of -15, -10, 5 and 0° are shown by fig. 34a,b,c and d for the symmerical square pitched rod array (p/d = 1.107).

It is apparent that the level of the advection, or balance term, is small for each radial traverse. Additionally, the magnitude of the azimuthal Reynolds shear stress component, for the traverse at 0° and $y/\hat{y} = 1.0$, becomes higher than either the axial pressure term or the radial Reynolds shear stress (fig. 34d). This term becomes of decreasing significance as θ changes between 0 and -15°, with the azimuthal gradient changing sign for the radial traverse at -15° (fig. 34a).

For all traverses shown, however, the axial momentum balance term is less than 1 p.u., when normalized by the factor $(\tau(\theta) \cdot \hat{y})$. It is illuminating to relate this to the maximum possible secondary flow velocity at selected traverse angles. For traverses at 0 and 45° in the large square pitch rod array, (section 3.1), W is zero because of the symmetry requirements. An approximate but feasible parabolic velocity distribution is proposed for V along these traverse angles, with a maximum value of $\hat{V}$. This distribution satisfies the boundary conditions (zero at the wall and at $y = \hat{y}$), and could be possible for either the notional single secondary flow cell (fig. 3) or multiple cells.

The approximate analytic integral in Appendix A shows, for a 1
p.u. out of balance at the subchannel centre line,

$$\frac{\hat{V}}{v^*(\theta)} = \frac{1}{4A} \cdot \frac{1}{(\frac{R}{2\hat{y}} + \frac{1}{6})} \qquad (10)$$

where A is the law of the wall coefficient, taken to be 2.5 or the
Nikuradse /34/ value. The other part of the ratio is a pure geome-
tric factor, depending on the subchannel geometry (triangular or
square array) and the traverse angle (0 or 45° for the square
pitch array).

To releate $\hat{V}$ to the maximum axial velocity $\hat{U}(r,\theta)$ for the relevant
traverse angle, the ratio of $(V^*(\theta)/\hat{U}(r,\theta))$ is needed.

The ratio for the extended Reynolds number survey /28/ in the
square pitch rod array is summarized in table 2.

Reynolds No. (x10³)	θ°	$v^*(\theta)/\hat{U}(r,\theta)\%$
22.6	0	7.1
22.6	15	6.5
22.6	45	5.4
133.0	0	5.0
133.0	15	4.8
133.0	45	4.2
207.6	0	4.6
207.6	15	4.7
207.6	45	4.0

Table 2

It can be seen from table 2 that there is a Reynolds number effect on this ratio, with the values for the rod gap reducing more rapidly than the 45° traverse for increasing Reynolds numbers. However, an average value may be taken as 5 %.

Substitution of these levels in equation 10 ·shows that, for a traverse at 0°, 1 p.u. out of balance implies a ratio of $\hat{V}/\hat{U}(r,\theta)$ of 0.1 %. This level is clearly neglegible, and may be compared to the approximately 25 % level of the cyclic component of the azimuthal turbulent velocity component w, established experimentally in the wall bounded rod array at a p/d ratio of 1.036. For the traverse at 45° in the symmetrical four rod subchannel (p/d = 1.107), a 1 p.u. out of balance at the centre-line of the duct implies the ratio $(\hat{V}/\hat{U}(r,\theta)$ to be 0.5 %. The analysis also predicts that the advection integral or balance component should monotonically increase from the rod wall to $\hat{y}$ = 1, for the duct symmetry boundaries.

5.3 Axial velocity and Secondary flow components

Consideration of the axial vorticity equation 6 (section 3.2), shows that the production term, P_2, appears to be far from zero in the rod gap area for the experimental data presented. This is the major source term, used in the numerical studies of developed rod bundle flow, for the production of an axial vorticity component /9,11,12/. However, the experimental measurements and axial momentum balance analysis show neglegible evidence of secondary flow velocities V and W. Instead the data shows the development of a very energetic large scale, and for very small p/d or w/d ratios, essentially periodic azimuthal turbulent velocity component w. This component becomes progressively more energetic in the centre of the rod gap as the rod spacing is reduced, and eventually becomes of greater intensity than the axial turbulent velocity component.

The high levels of the azimuthal Reynolds shear stress component $(-\rho\overline{uw})$ have been shown to be associated, for the wall bounded rod array spaced at a p/d ratio of 1.036, with the large scale periodic component of w and u. It is only at very small p/d ratios that the large scale structure becomes so evident. However it is probable that there is a progressive development of the process whereby energy is selectively transfered to the azimuthal turbulent velocity component w, as the p/d or w/d ratio is reduced. The development of a non-zero planar Reynolds shear stress component for the symmetrical four rod (p/d = 1.107) subchannel is readily explained in terms of the cyclic large scale w component. The w component is directed essentially along the subchannel centre line (fig. 35), or the y axis for a rod gap centre cartesian co-ordinate system. If this is measured in a rod centered co-ordinate system, fig. 35, and it is assumed that w is the major turbulent component in the axial plane and the rod gap region as the experimental data suggests in the rod centered co-ordinates for $|\theta| > 0^{\circ}$ the w fluctuation is reflected into both the azimuthal and radial components as $w \cos\theta \cdot w \sin\theta$.

The correlation is non zero for $|\theta| > 0^{\circ}$, and is $-\dfrac{\overline{w^2}}{2} \sin2$. The maximum value does not occur at 45° as this relation suggests, as the cyclic w component does not extend beyond 35°. The analysis also shows $-\rho\overline{vw}$ to be antisymmetric with respect to the symmetry boundary ($\theta = 0^{\circ}$), as is confirmed by the data for the interior subchannel rig.

The fluid mechanism whereby the transverse (in a cartesian co-ordinate system centered at the rod gap middle) turbulent velocity component w is excited to the extreme levels found in narrow rod gaps is not yet clear. However, the mechanism may involve cyclic pressure fluctuations between the interconnected subchannels. The normal generation mechanisms of turbulence in duct flows /38/ are unlikely to account for the selective excitation of the w component.

The existence of this cyclic process has only been shown to apply in rod clusters of strictly limited extent. If generally applicable to the large arrays employed by power reactors, it represents an effective mechanism of intersubchannel mixing.

6. Conclusion

The turbulent fluid structure in the rod gap region for closely spaced rod arrays shows the presence of a highly energetic azimuthal, or transverse turbulent velocity component directed through the rod gap. At low p/d or w/d ratios the component becomes essentially periodic in frequency, and is highly corre-lated across the rod gap central symmetry line (θ = 0°). No significant secondary flow cells were found to be present in the rod gap region either by direct measurement, or by consideration of the axial momentum balance.

Acknowledgement

References

/1/ Brundrett, E. and Baines, W.
     The production and diffusion of vorticity in duct flow
     J. Fluid Mech. Vol. 19 (1964), p. 375

/2/ Gessner, F.B.
     The origin of secondary flow in turbulent flow along a
     corner
     J. Fluid Mech. Vol. 58 (1973), p. 1

/3/ Launder, B.E. and Ying, Y.M.
     Secondary flows in ducts of square cross-section
     J. Fluid Mech. Vol. 54 (1972), p. 115

/4/ Aly, A.M.M, Trupp, A.C. and Gerrard, A.D.
     Measurement and prediction of fully developed turbulent flow
     in an equilateral triangular duct
     J. Fluid Mech. Vol. 85 (1978), p. 57

/5/ Galbraith, K.P. and Knudsen, J.G.
     Turbulent mixing between adjacent channels for single phase
     flow in a simulated rod bundle
     Am. Inst. Chem. Eng. Vol. 68 (1972), p. 90

/6/ Kjellström, B.
     Studies of turbulent flow parallel to a rod bundle of trian-
     gular array
     Atkiebolaget Atomenergi Report AE-487 (1974)

/7/ Trupp, A.C. and Azad, R.S.
     Turbulent flow in triangular rod bundles
     Nuc. Engng. Des. Vol. 32 (1975), p. 47

/8/ Rowe, D.S.
Measurements of turbulent velocity, intensity and scale in
rod bundle flow channels
BNWL-1736 (1973)

/9/ Carajilescov, P. and Todreas, N.E.
Experimental and analytical study of axial turbulent flows
in an interior subchannel of a bare rod bundle
Paper HT/51, ASME Winter annual meeting (1975)

/10/ Launder, B.E. and Ying, Y.M.
Prediction of flow and heat transfer in ducts of square
cross-section
Heat and Fluid Flow, Vol. 3 (1973), p. 115

/11/ Trupp, A.C. and Aly, A.M.M.
Prediction of turbulent flow in finite rod clusters
J. Fluids Eng. Vol. 10 (1979), p. 354

/12/ Benodekar, R.W. and Date, A.W.
Prediction of turbulent flow in finite rod clusters
2nd Symposium on turbulent shear flows, London (1979)

/13/ Seale, W.J.
Turbulent diffusion of heat between connected flow passages
Nucl. Engng. Des. Vol. 54 (1979), p. 183

/14/ Rehme, K.
Strömungsuntersuchungen an einem asymmetrischen Stabbündel
(W/D = 1.118), KfK-Bericht 3318 (1982)

/15/ Rehme, K.
Strömungsuntersuchungen an einem asymmetrischen Stabbündel
(W/D = 1.026), KfK-Bericht 3324 (1982)

/16/ Rehme, K.

Distributions of velocity and turbulence in a parallel flow
along an asymmetric rod bundle
Nuclear Technology, Vol. 59 (1982), p. 148

/17/ Rehme, K.

Distributions of velocity and turbulence for parallel flow
along an asymmetric rod bundle
Paper presented at the 1st Specialists Meeting organized
by the IAHR Committee on Liquid Metals Thermal-Hydraulics,
MIT, Cambridge, October 5 - 6 (1981)

/18/ Rehme, K.

Strömungsuntersuchungen an einem asymmetrischen Stabbündel
(W/D = 1.048)
KfK-Bericht 3069 (1980)

/19/ Rehme, K.

Strömungsuntersuchungen an einem asymmetrischen Stabbündel
(W/D = 1.096)
KfK-Bericht 3047 (1980)

/20/ Rehme, K.

Strömungsuntersuchungen im Wandkanal eines Stabbündels
(P/D = 1.036, W/D = 1.072)
KfK-Bericht 3361 (1982)

/21/ Rehme, K.

Untersuchungen zur Turbulenzstruktur in einem Wandkanal eines
Stabbündels (P/D = 1.07)
KfK-Bericht 2983 (1980)

/22/ Rehme, K.

Turbulente Strömung in einem Wandkanal eines Stabbündels
KfK-Bericht 2617 (1978)

/23/ Rehme, K.
Geschwindigkeits- und Turbulenzverteilungen in einem Wand-
kanal eines Stabbündels
KfK-Bericht 2637 (1978)

/24/ Patel, V.C.
Calibration of the Preston tube and limitations on its use in
pressure gradients
J. Fluid Mech. Vol 23 (1965), p. 185

/25/ Hooper, J.D.
Fully developed turbulent flow through a rod cluster
Ph. D. Thesis, University of N.S.W., Sydney, Australia (1980)

/26/ Hooper, J.D.
The calculation of fully developed turbulent and laminar
single phase flow in four rod subchannels
A.A.E.C. E-351 (1975)

/27/ Hooper, J.D.
Developed single phase turbulent flow through a square pitch
rod cluster
Nucl. Engng. Des. Vol 60 (1980), p. 365

/28/ Hooper, J.D., Wood, D.H. and Crawford, W.J.
Developed single phase turbulent flow through a square
pitched rod cluster for an extended range of Reynolds numbers
Australian Atomic Energy Report (to be published)

/29/ Hinze, J.O.
Turbulence
McGraw-Hill (1975)

/30/ Wood, D.H.

The equations describing secondary flow in cylindrical

polar co-ordinates

University of Newcastle T.N.-F.M. 61, Newcastle, Australia

(1981)

/31/ Perkins, H.J.

The formation of streamwise vorticity in turbulent flow

J. Fluid Mech. Vol 44 (1970), p. 721

/32/ Rehme, K.

Experimental investigations of turbulent flow in gaps of rod

bundles

IAHR 2nd International Specialists meeting on thermal-hydrau-

lics in LMFBR rod bundles, Rome (1982)

/33/ Eifler, W., and Nijsing, R.

VELASCO Velocity field in asymmetric rod configurations

Report EUR-4550e (1973)

/34/ Nikuradse, J.

Gesetzmäßigkeiten der turbulenten Strömung in glatten Rohren

VDI Forsch. Heft Nr. 356 (1932)

/35/ Laufer, J.

The structure of turbulence in fully developed pipe flow

NACA report 1174 (1954)

/36/ Lawn, C.J.

The determination of the rate of dissipation in turbulent

pipe flow

J. Fluid Mech. Vol 48 (1971), p. 477

/37/ Hooper, J.D.

An investigation of the mechanism of intersubchannel momentum transfer for closely spaced rod arrays
IAHR 2nd International specialists meeting on thermal-hydraulics in LMFBR rod bundles, Rome (1982)

/38/ Launder, B.E., Reece, G.J. and Rodi, W.

Progress in the development of a Reynolds stress turbulence closure
J. Fluid Mech. Vol. 68 (1975), p. 537

Notation

A	Constant in logarithmic law of the wall
B	Constant in logarithmic law of the wall
$C_{u_i v_j}$	Correlation function between designated turbulent velocity components at locations i and j
d	rod diameter
p	rod pitch
g	rod to wall gap width
p/d	rod pitch to diameter ratio
w/d	rod wall to diameter ratio (1 + g/d)
R	rod radius
U	mean axial velocity
u,v,w	turbulence components in either cylindrical (z,r,θ) or cartesian (z,x,y) co-ordinate system
u^+	Dimensionless mean velocity
V,W	Mean velocity components in (z,r,θ) or (z,x,y)
v^*	friction velocity
y	wall distance
y^+	dimensionless wall distance

$\mathring{y}$ distance from rod wall to subchannel centre-line of symmetry

P mean static pressure

P_1, P_2, P_3, P_4 Production terms for streamwise vorticity

μ dynamic viscosity

ρ air density

τ wall shear stress

Ω vorticity

Φ mean static pressure function

Superscripts

$\overline{}$ time averaged quantity

$\hat{}$ peak value

$'$ R.M.S. value

Appendix A

Estimation of secondary flow velocities by the axial momentum equation

For developed flow conditions, the axial momentum equation (2) (Section 3.1) reduces to:

$$\rho \left(V \frac{\partial U}{\partial r} + \frac{W}{r} \frac{\partial U}{\partial \theta}\right) = - \frac{\partial P}{\partial z} + \mu \left[\frac{1}{r} \frac{\partial}{\partial r} \left(r \frac{\partial U}{\partial r}\right) + \frac{1}{r^2} \frac{\partial^2 U}{\partial \theta^2}\right]$$

$$- \rho \left[\frac{1}{r} \frac{\partial (r \overline{uv})}{\partial r} + \frac{1}{r} \frac{\partial \overline{uw}}{\partial \theta}\right] \tag{A1}$$

The axial gradient of the static pressure is constant at C_1, and the unknown secondary flow terms are contained by the total fluid derivative term. If the value of the viscous term only at the wall is considered of significance (Wood /30/), a reasonable approximation in high Reynolds number internal duct flows, this term may be approximated by:

$$\frac{1}{r} \frac{\partial}{\partial r} (r \tau (\theta))$$

The radial gradient of the mean axial velocity is assumed to dominate the viscous term at the rod wall, and $\tau(\theta)$ is the wall shear stress acting in the r-z plane.

Premultiplication of equation by r, and integration in the radial direction between the rod wall R and R+y, where y is the distance of the fluid point to the wall gives:

$$\rho \int_R^{R+y} r \left(V \frac{\partial U}{\partial r} + \frac{W}{r} \frac{\partial U}{\partial \theta}\right) dr = - \frac{\partial P}{\partial z} \cdot \frac{y^2 + 2ry}{2} - R\tau(\theta)$$

$$- \rho \overline{uv} \cdot (y + R) - \rho \int_R^{R+y} \frac{\partial \overline{uw}}{\partial \theta} dr \tag{A2}$$

The secondary flow terms V and W are thus the only unknown terms in equation (A$_2$), in which all terms on the R.H. side are known or may be calculated from measured functions. The azimuthal gradient of the azimuthal shear stress is the most doubtful quantity to calculate, being the difference of experimental Reynolds stress terms. A central finite difference scheme was used for this component, and $-\rho\overline{uw}$ was assumed to vary linearly from zero at the rod wall to the first measured data value.

The momentum integral equation (A$_2$) was non-dimensionalized by division by $\tau(\theta)y$, where y is the wall distance to the subchannel centre line CD (fig. 3).

If no significant secondary flow components are present, the L.H. side of equation (A$_2$) is zero for the given angle, and the R.H. side should balance, for all wall distances y, to zero. As noted in Section 3.1, W is zero along radial traverses at 0 and 45° and V is zero at the wall, gap centre (point C) or subchannel centre (point B). In order to evaluate the level of V required to produce a 1 per unit out of balance level at the subchannel centre for the 45° traverse, or the 0° traverse at the rod gap centre, the following approximate evaluation of the advection integral is made:

$$V(r,\theta) = \hat{V} \, (y/\hat{y} - (y/\hat{y})^2) \qquad (A3)$$

The parabolic form of $V(r,\theta)$ for 0 and 45° satisfies the required boundary conditions for both traverse angles, being zero at the wall and duct centre-line BC.

The radial mean axial velocity distribution $U(r,\theta)$ is assumed to be given by the logarithmic law of the wall, an approximation close to the actual experimental values for the turbulent core region.

$$U(r,\theta) = (A \ln yv^*(\theta)/\nu + B) \cdot v^*(\theta) \qquad (A4)$$

The advection integral becomes

$$\rho \int_{R}^{R+\hat{y}} rV \frac{\partial U}{\partial r} \, dr = \frac{4A\hat{V}}{v^*(\theta)\hat{y}} \int_{0}^{\hat{y}} (R+y) \cdot \frac{1}{y} \cdot \left(\frac{y}{\hat{y}} - \left(\frac{y}{\hat{y}}\right)^2\right) dy$$

$$= \frac{4A}{\hat{y}} \cdot \frac{\hat{V}}{v^*(\theta)} \cdot \left[\frac{R}{2} + \frac{\hat{y}}{6} \right] \tag{A5}$$

For a 1 per unit out of balance,

$$\frac{\hat{V}}{v^*(\theta)} = \frac{1}{4A} \cdot \frac{1}{\left[\frac{R}{2\hat{y}} + \frac{1}{6} \right]} \tag{A6}$$
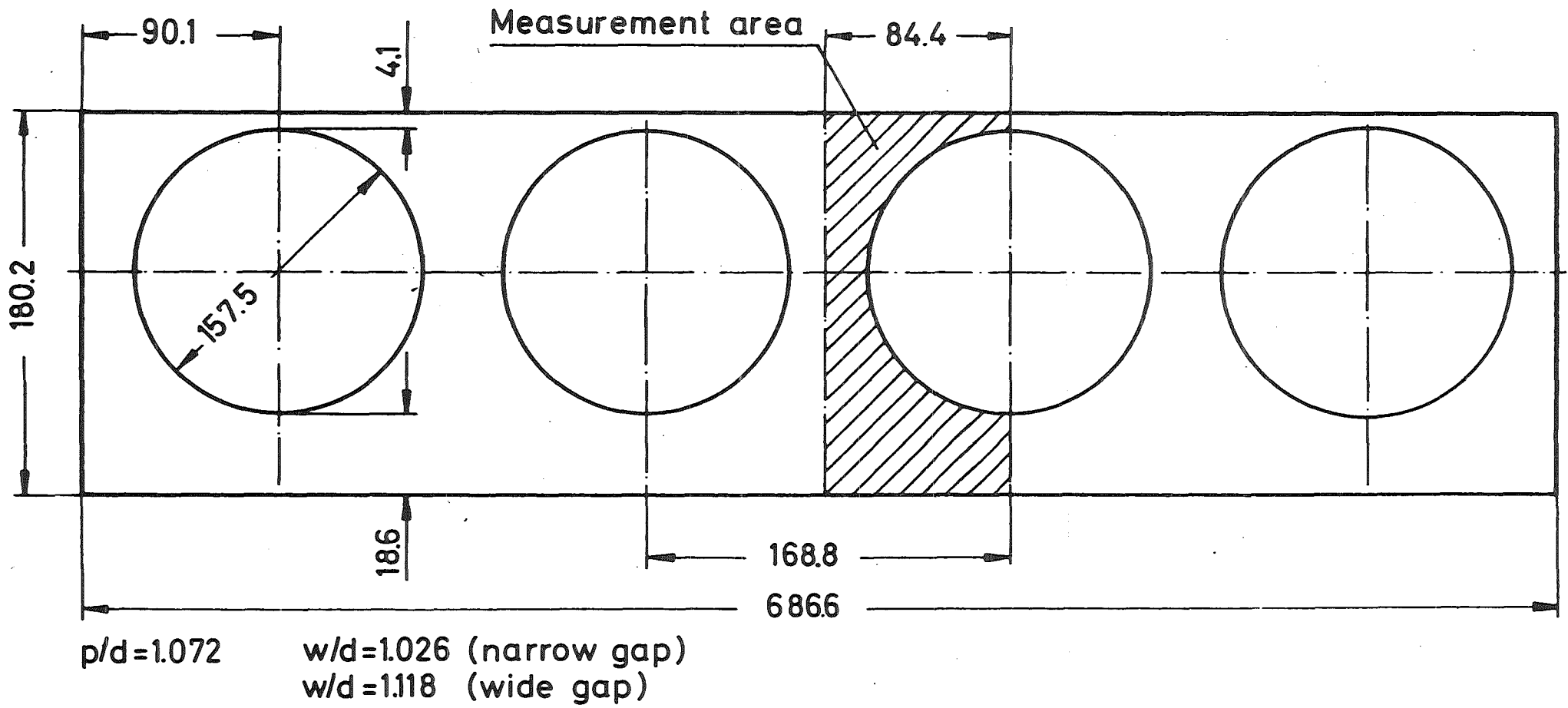
Fig. 1 Test Section 1: Wall bounded array
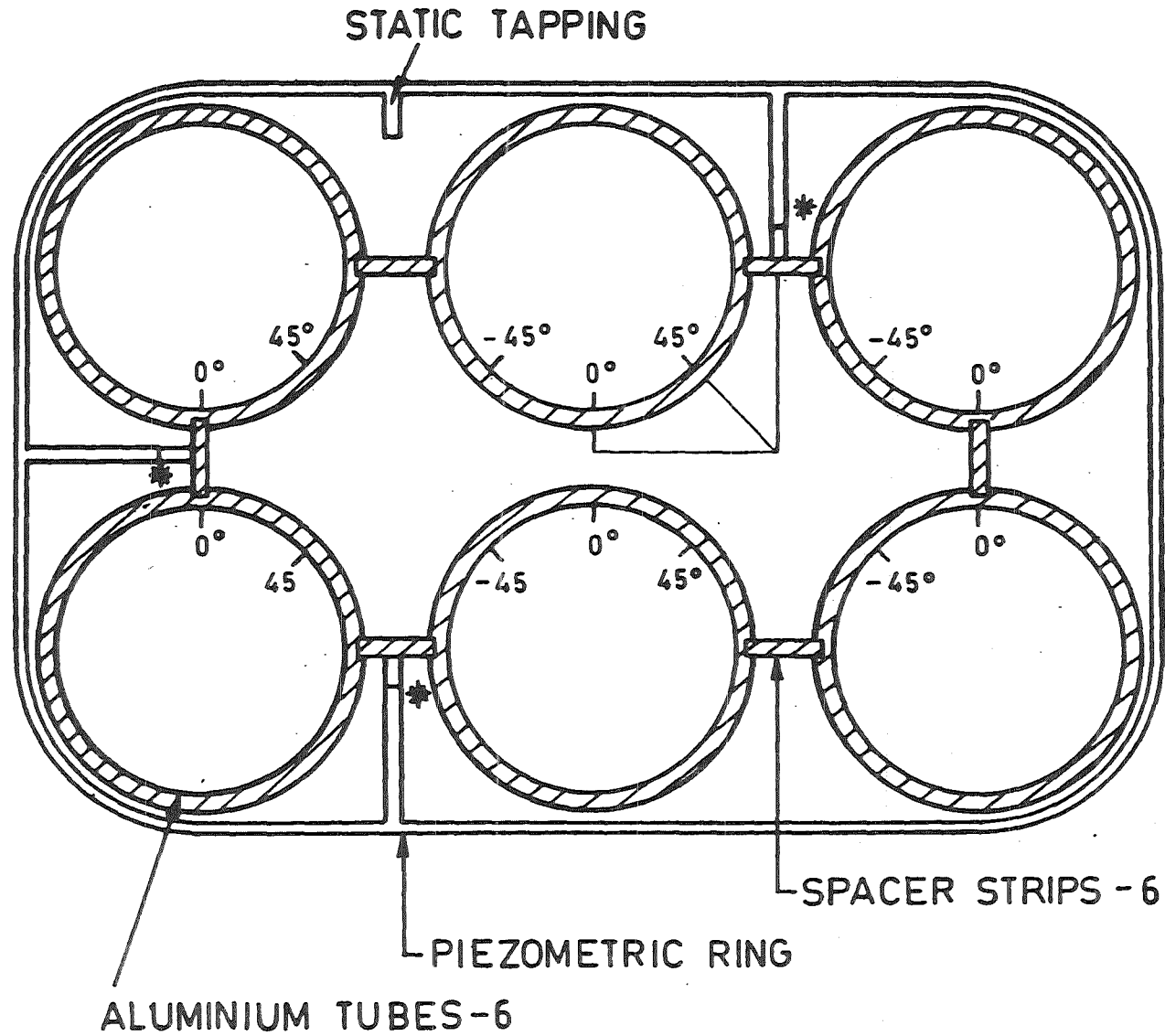
Fig. 2 Test Section 2: Symmetrical square pitch cluster
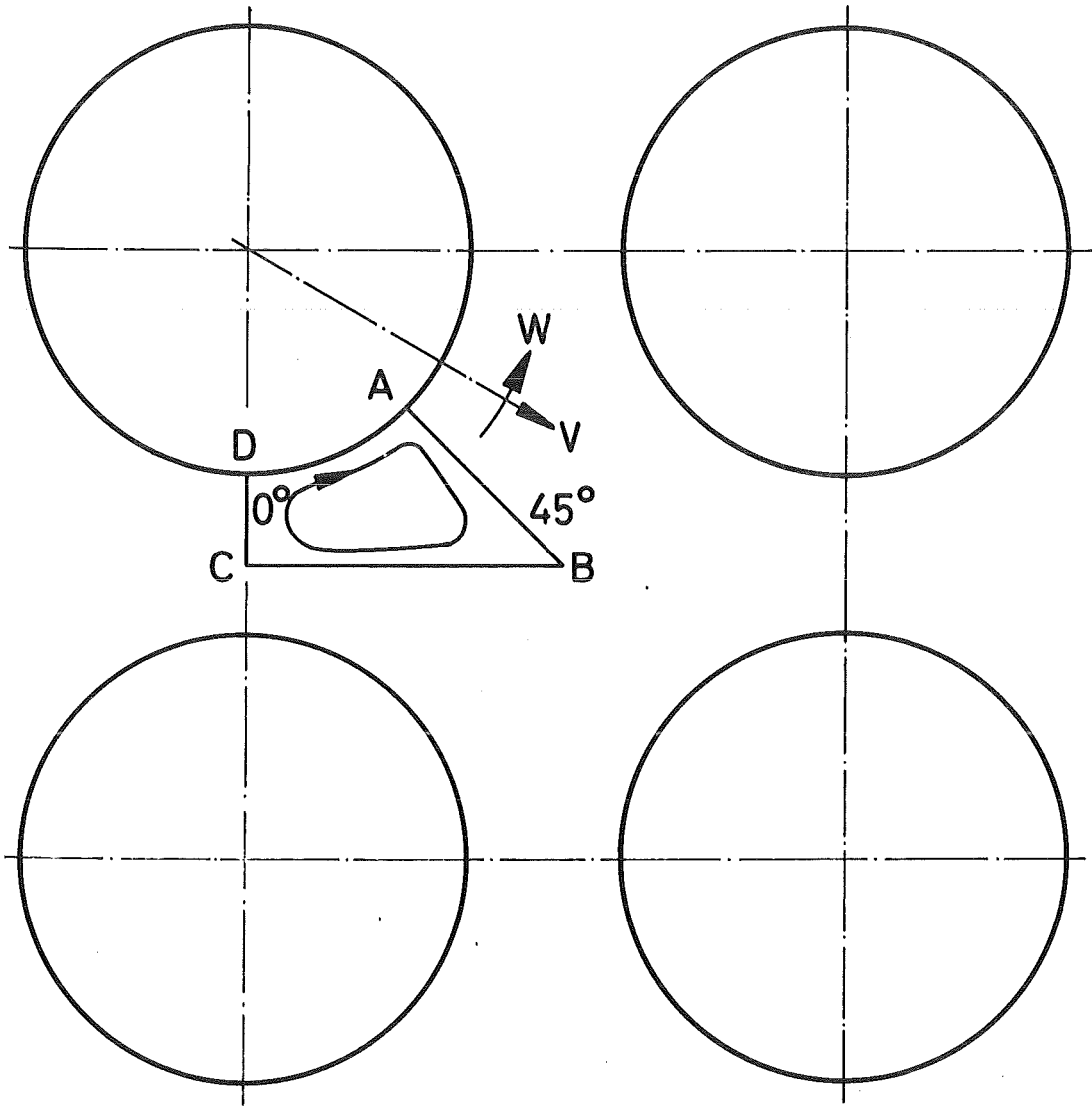
Symmetry zone of a large square-pitch
rod array. Direction for+V,W shown,
together with notional single
secondary flow cell.

Fig. 3   Symmetry zone of square pitch array
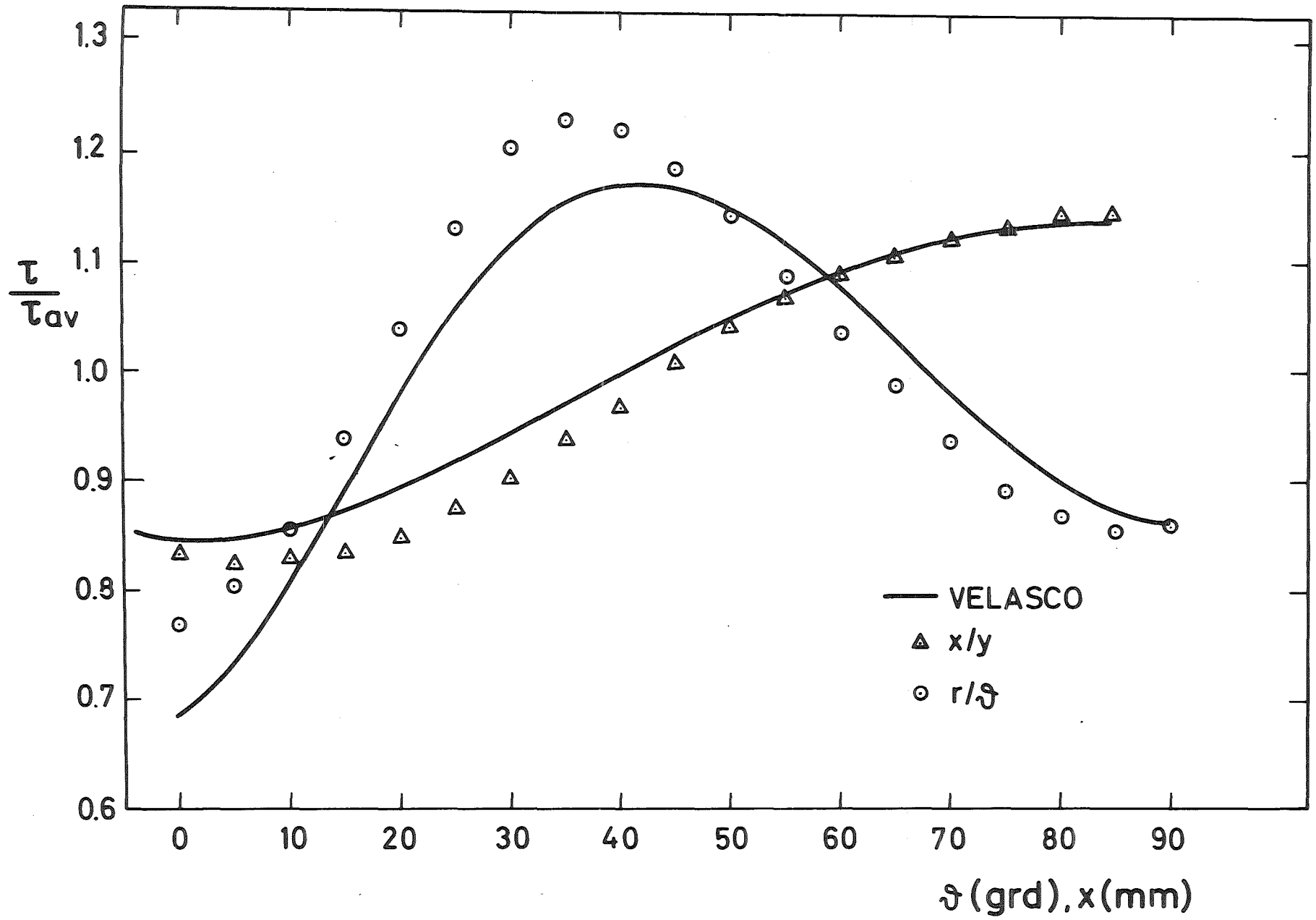
Fig. 4   Distribution of the wall shear stress: W/D=1.118
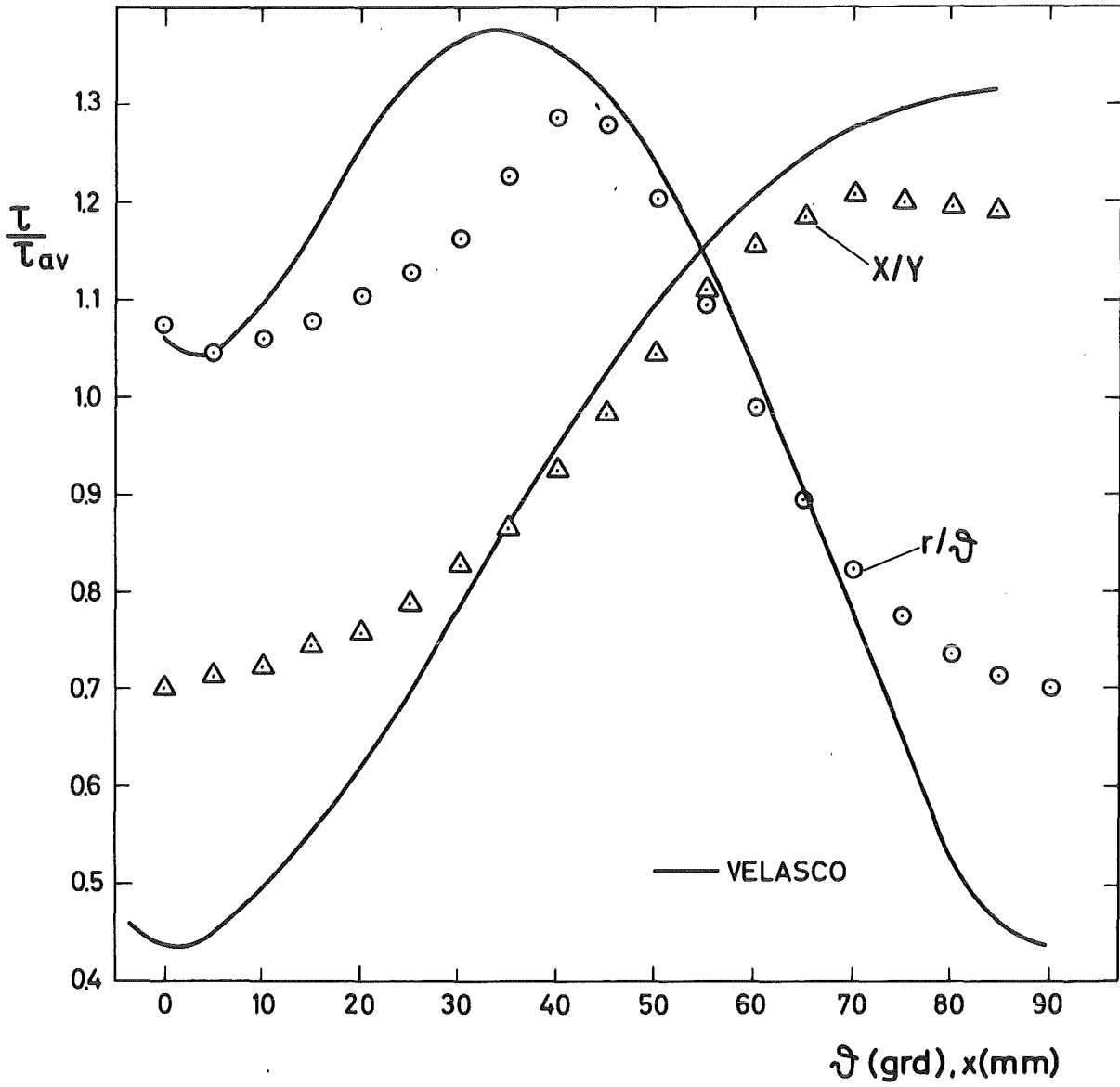
Fig. 5 Distribution of the wall shear stress: W/D=1.026
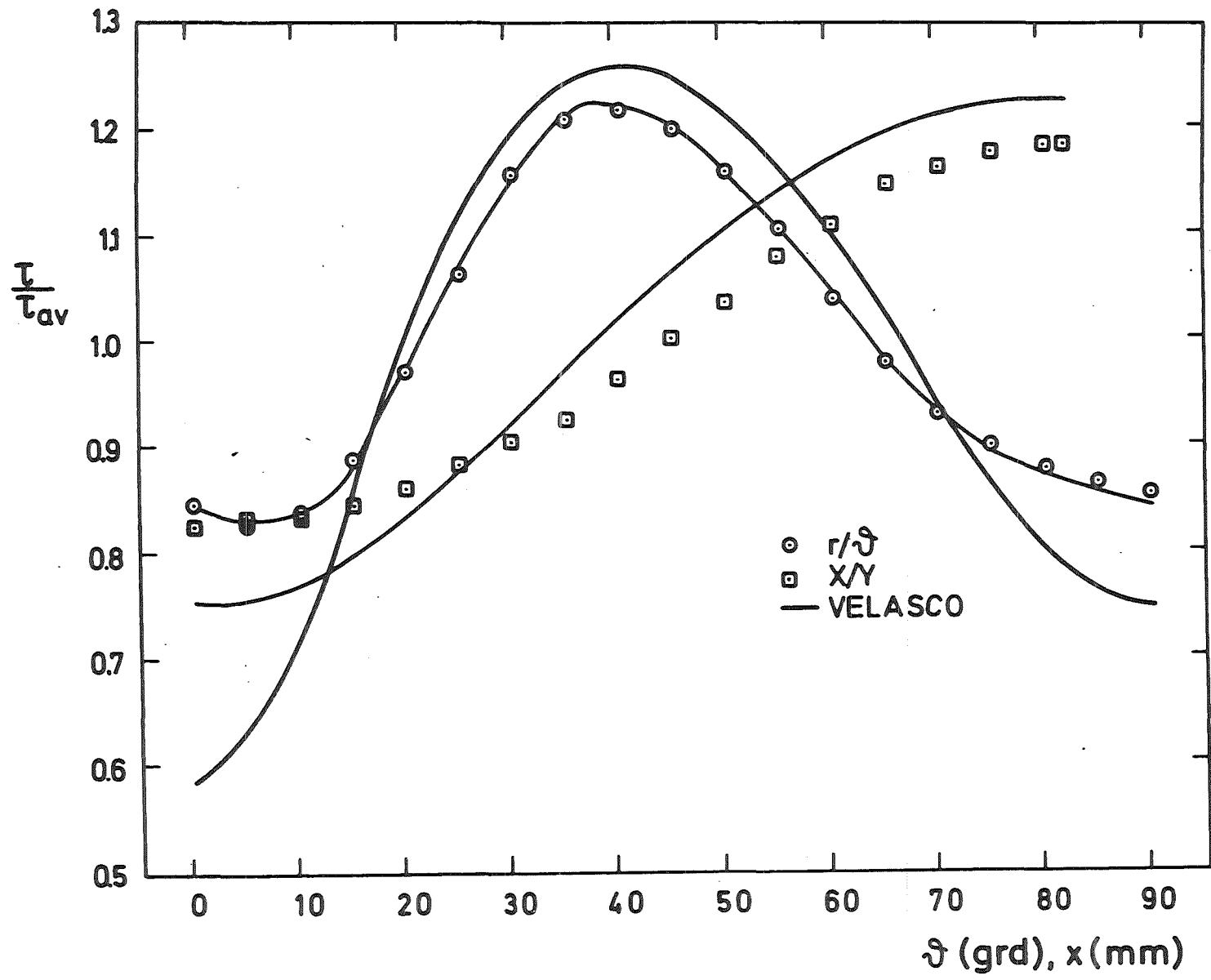
Fig. 6 Distribution of the wall shear stress: P/D=1.036
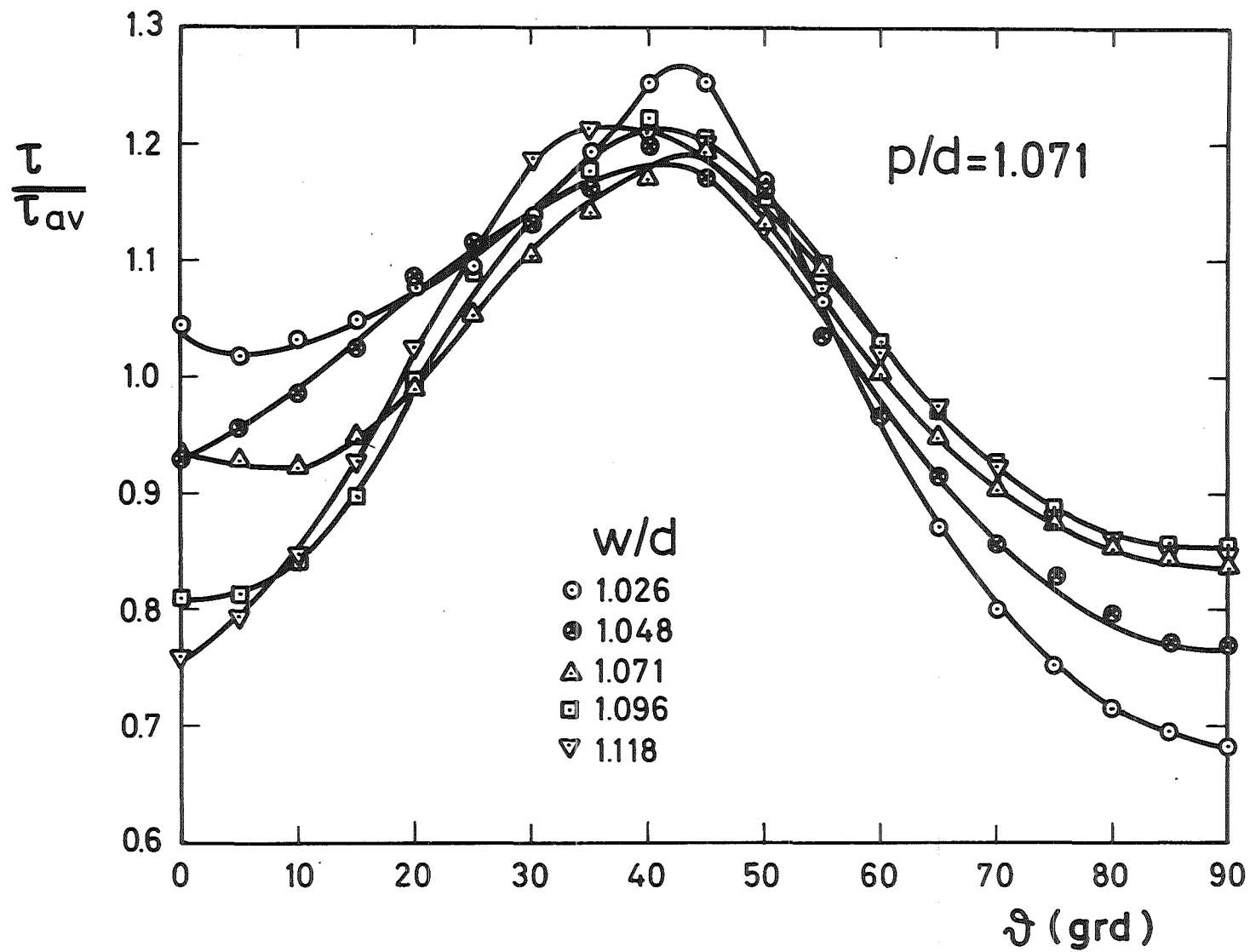
Fig. 7   Experimental wall shear stresses along the rod wall
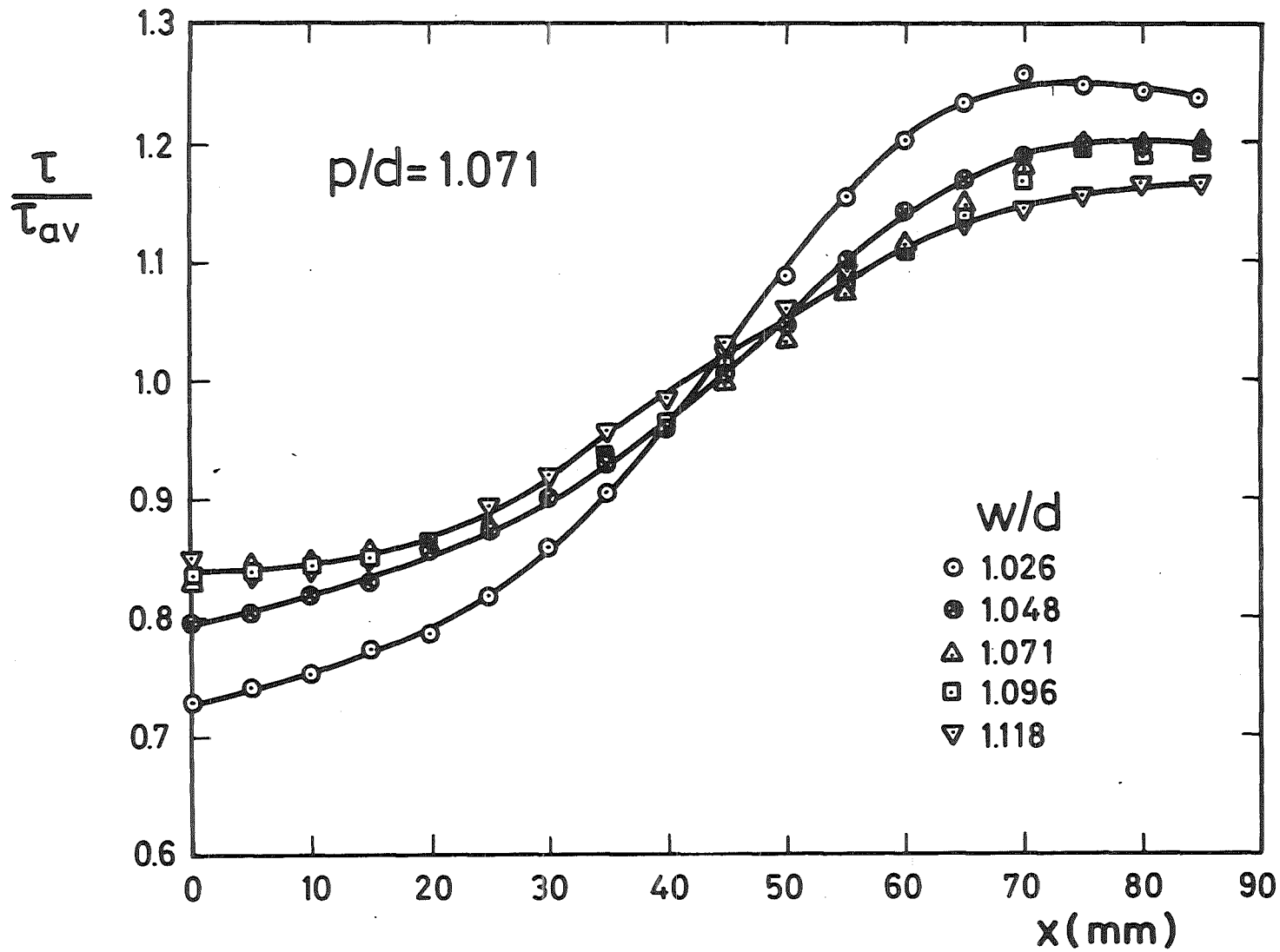
Fig. 8   Experimental wall shear stresses along the channel wall
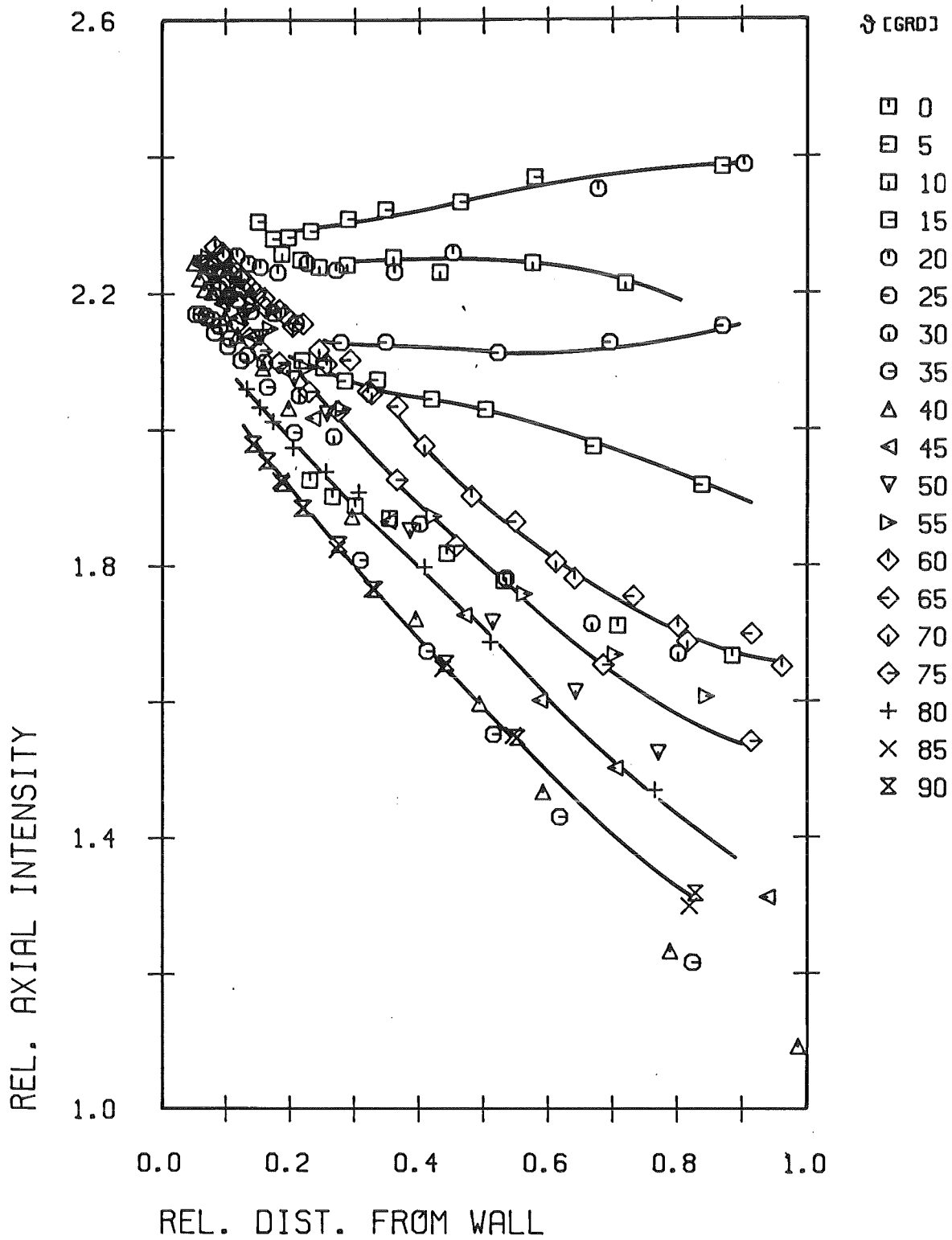
Fig. 9 Axial turbulence intensity: W/D=1.118
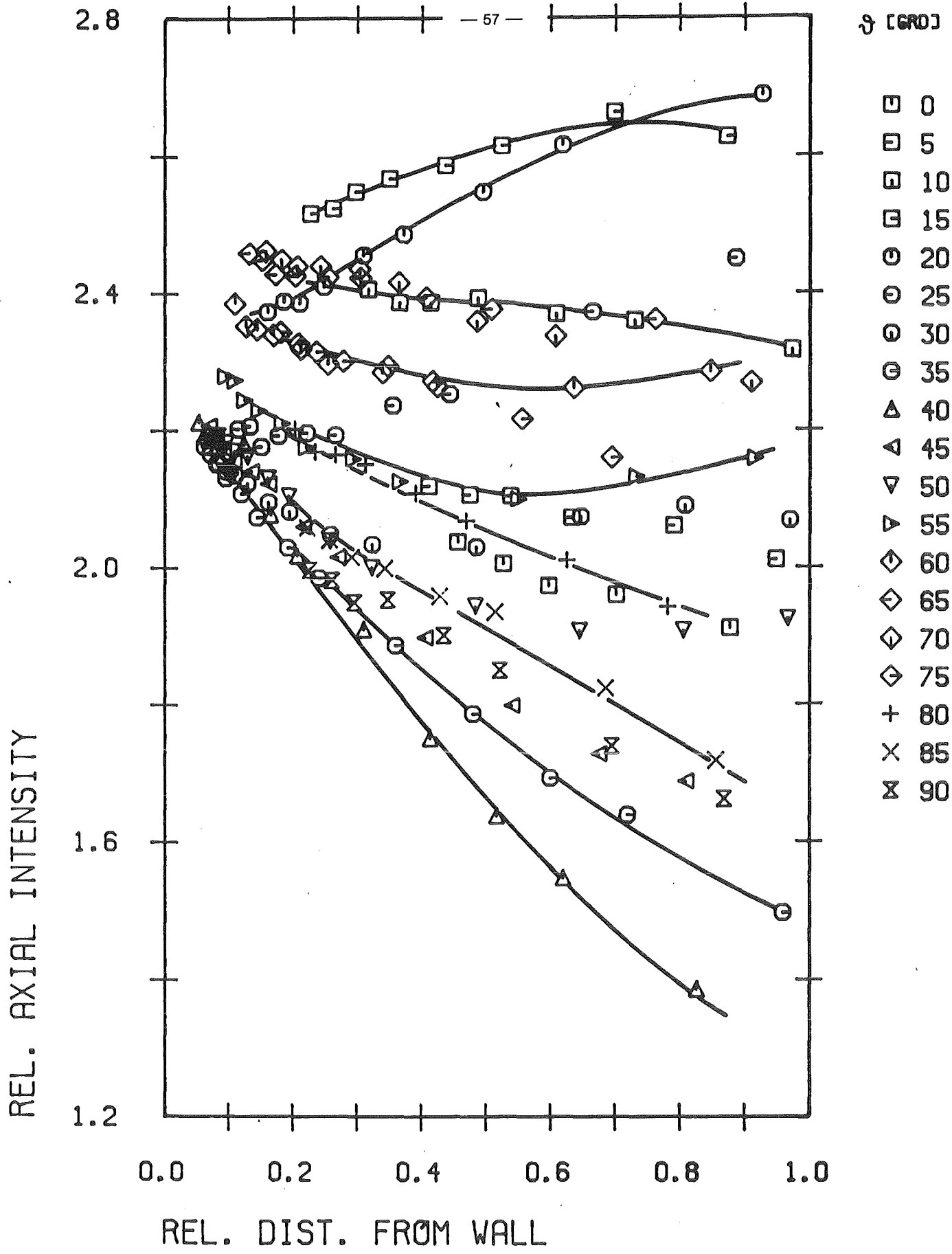
Fig. 10 Axial turbulence intensity: P/D=1.036
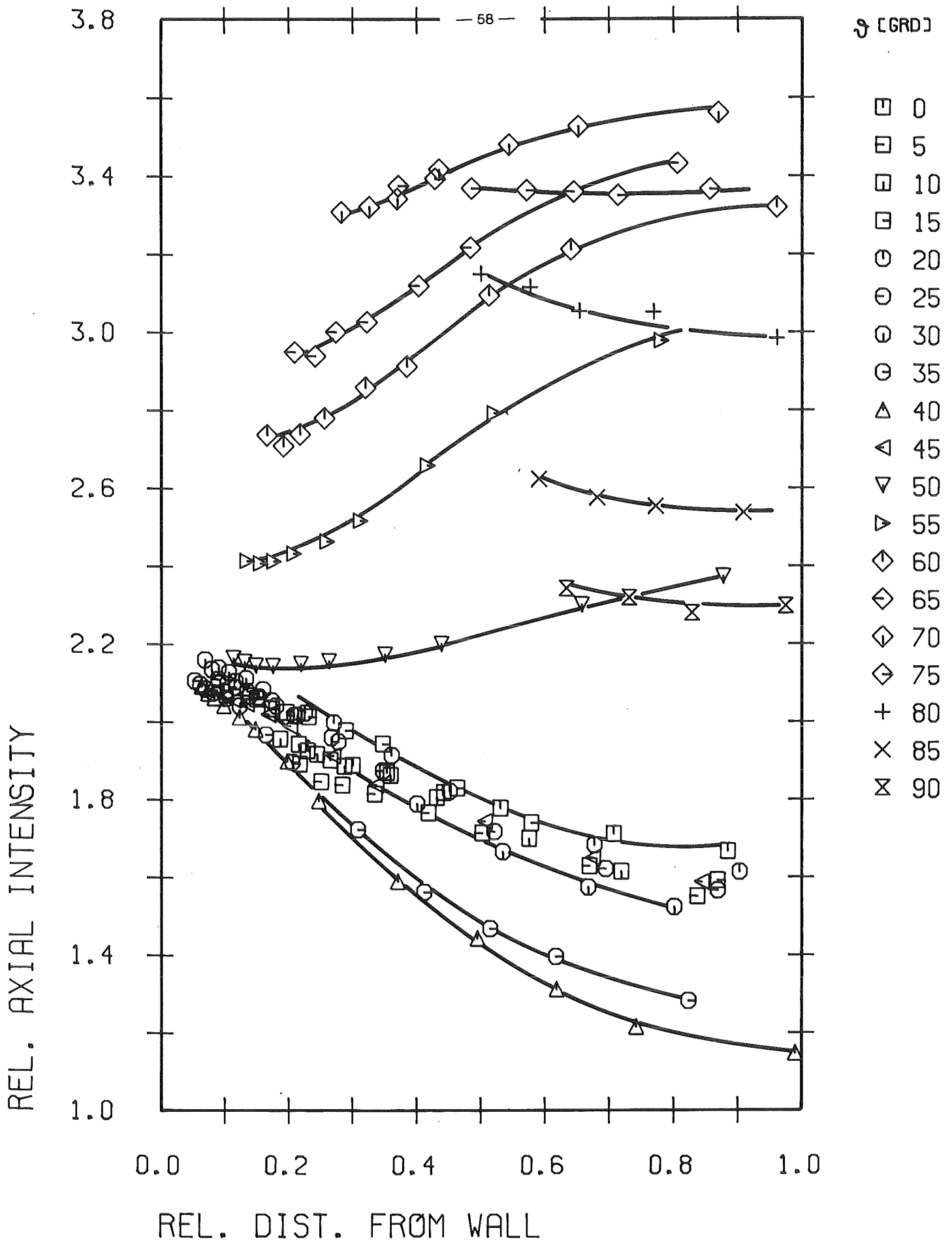
Fig. 11 Axial turbulence intensity: W/D=1.026
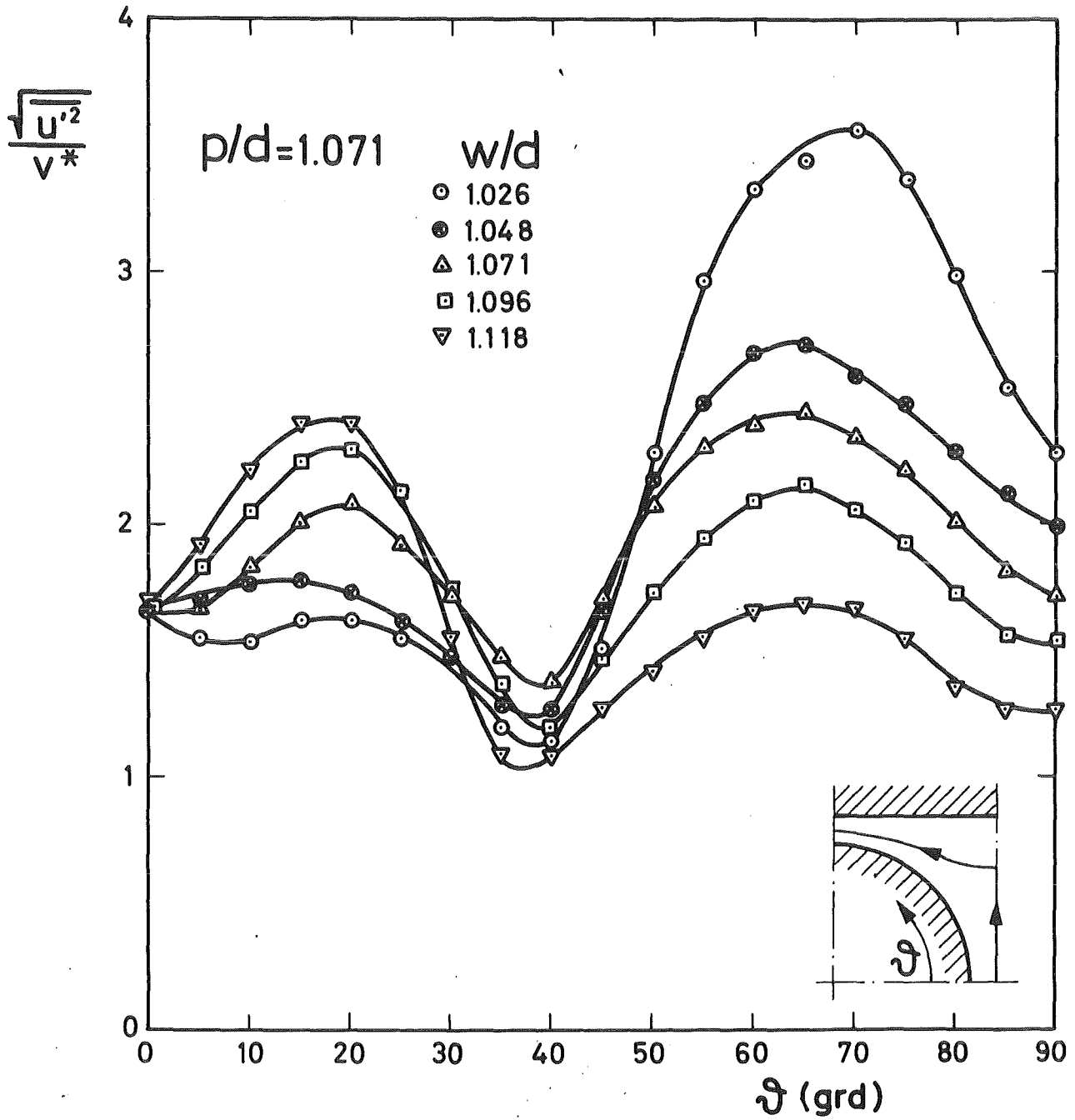
Fig. 12 Axial turbulence intensity along the line of
         maximum velocity
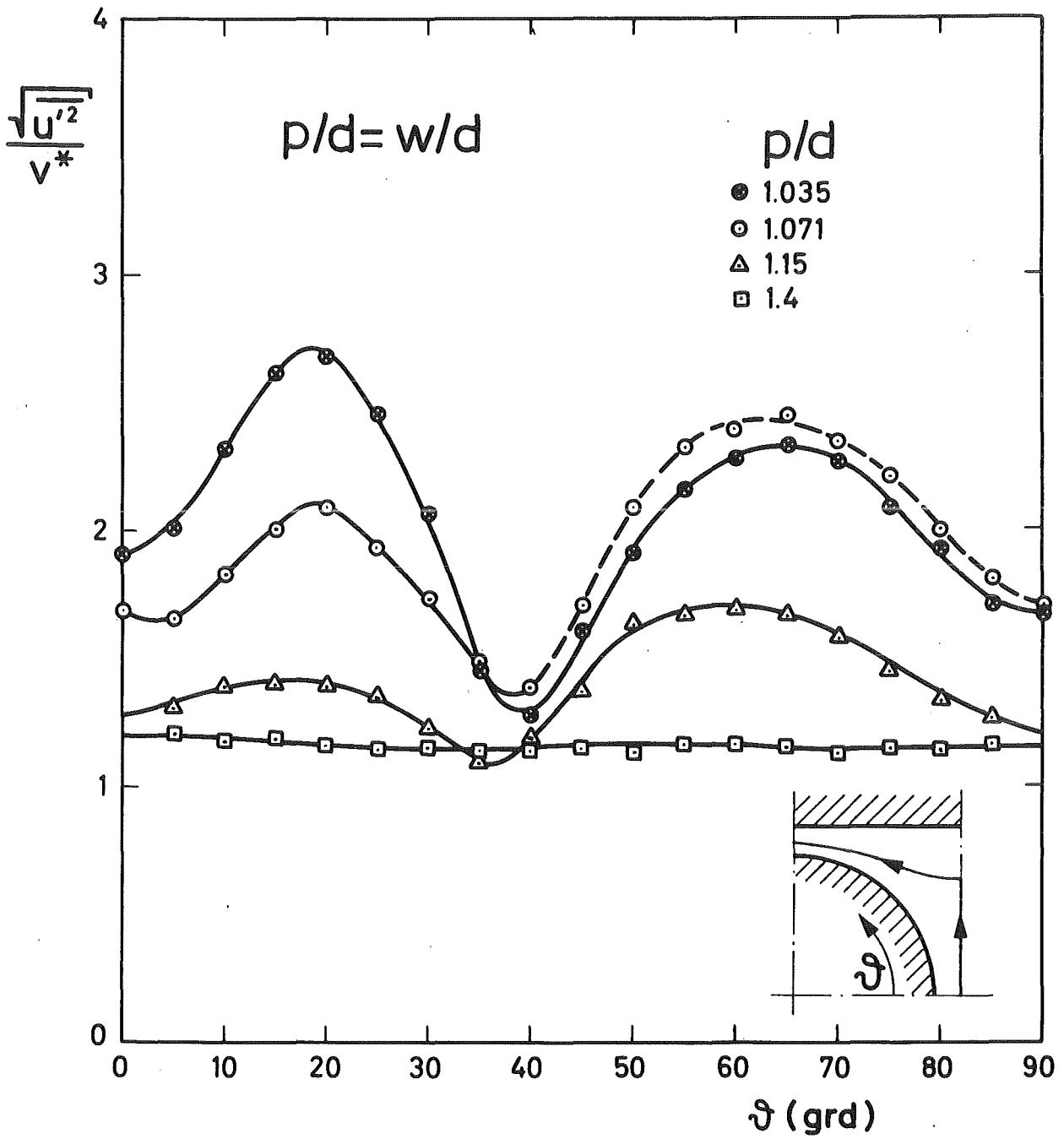
Fig. 13 Axial turbulence intensity along the line of maximum velocity
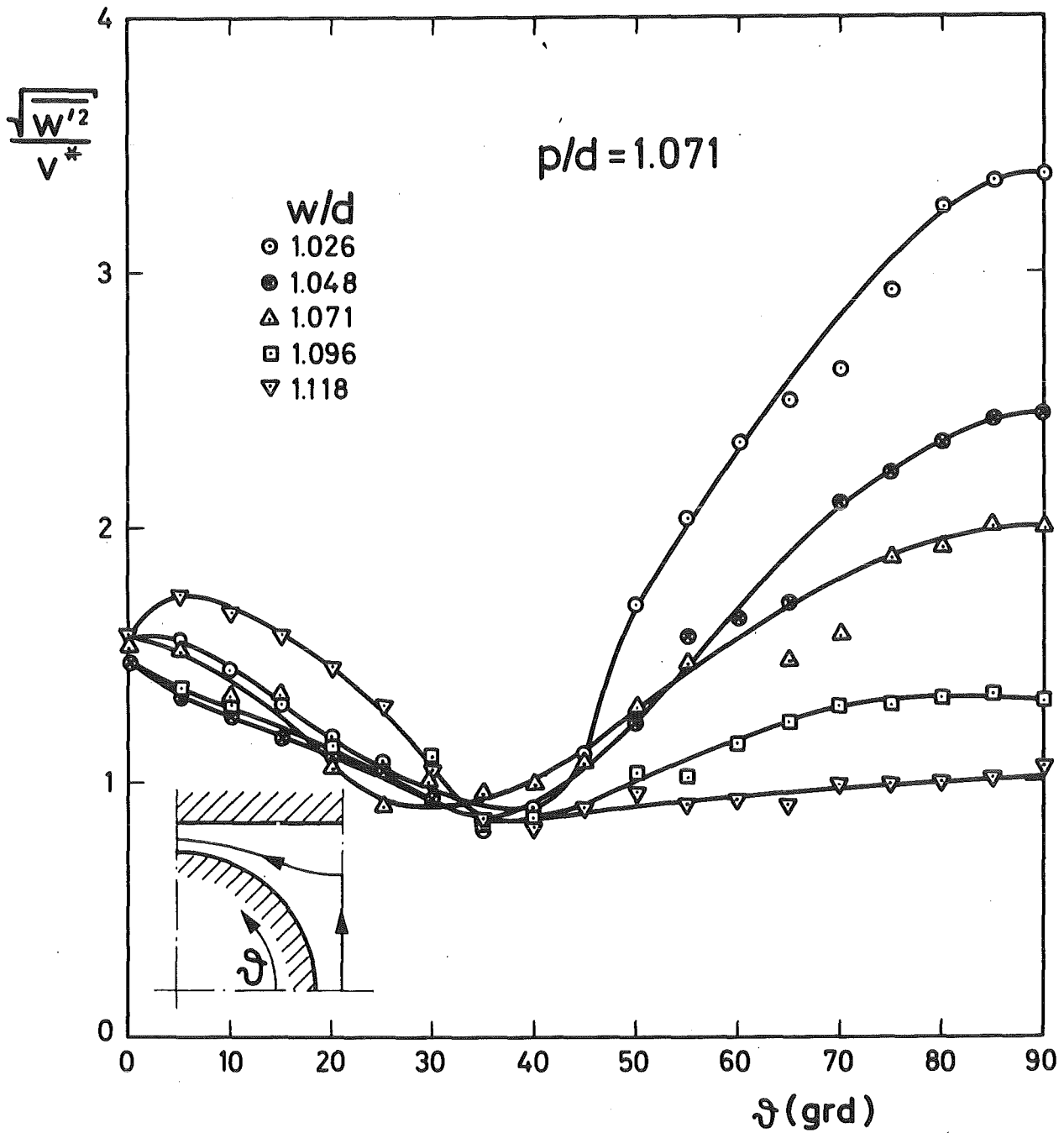
Fig. 14 Azimuthal turbulence intensity along the line
of maximum velocity
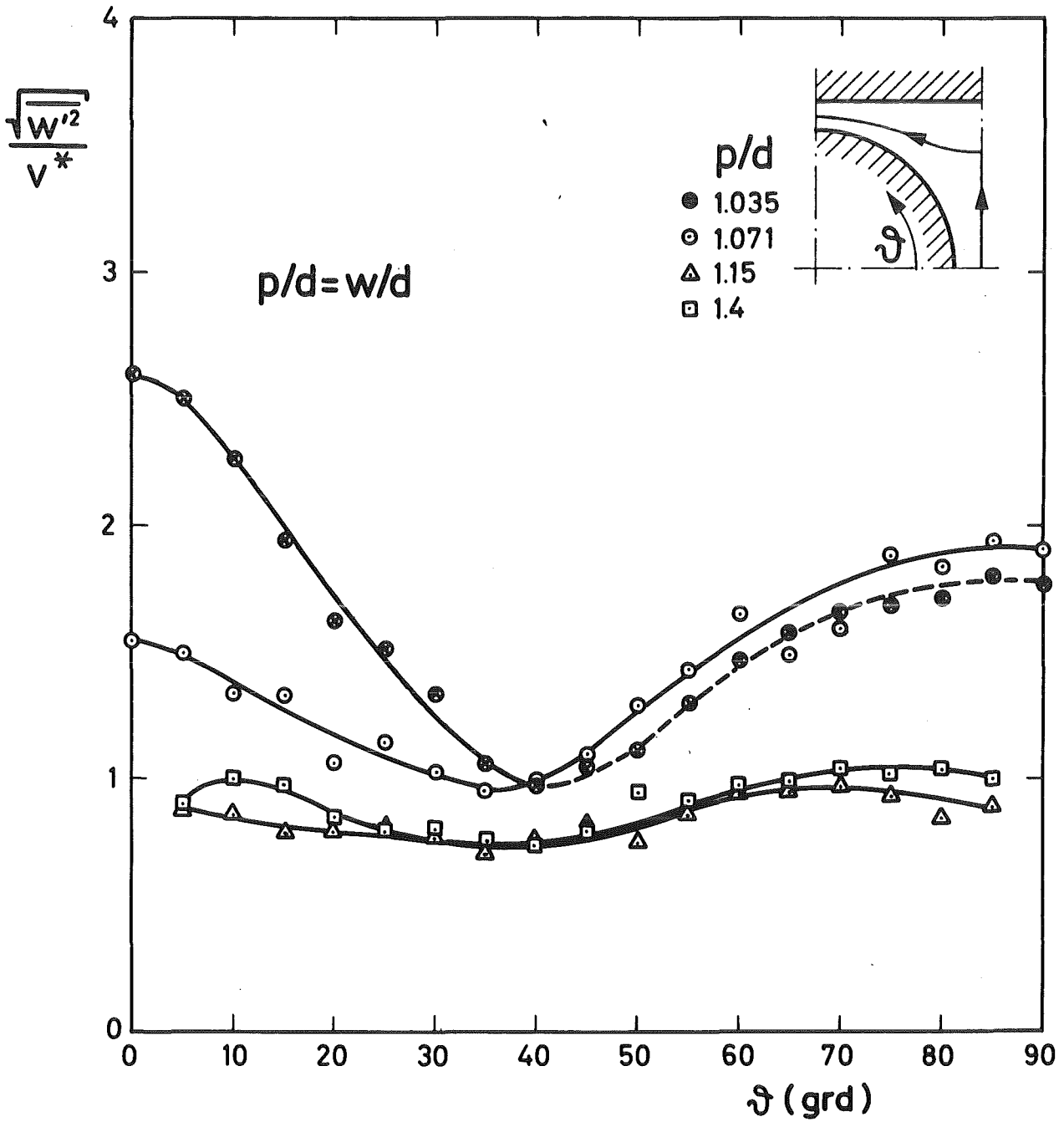
Fig. 15   Azimuthal turbulence intensity along the line
          of maximum velocity
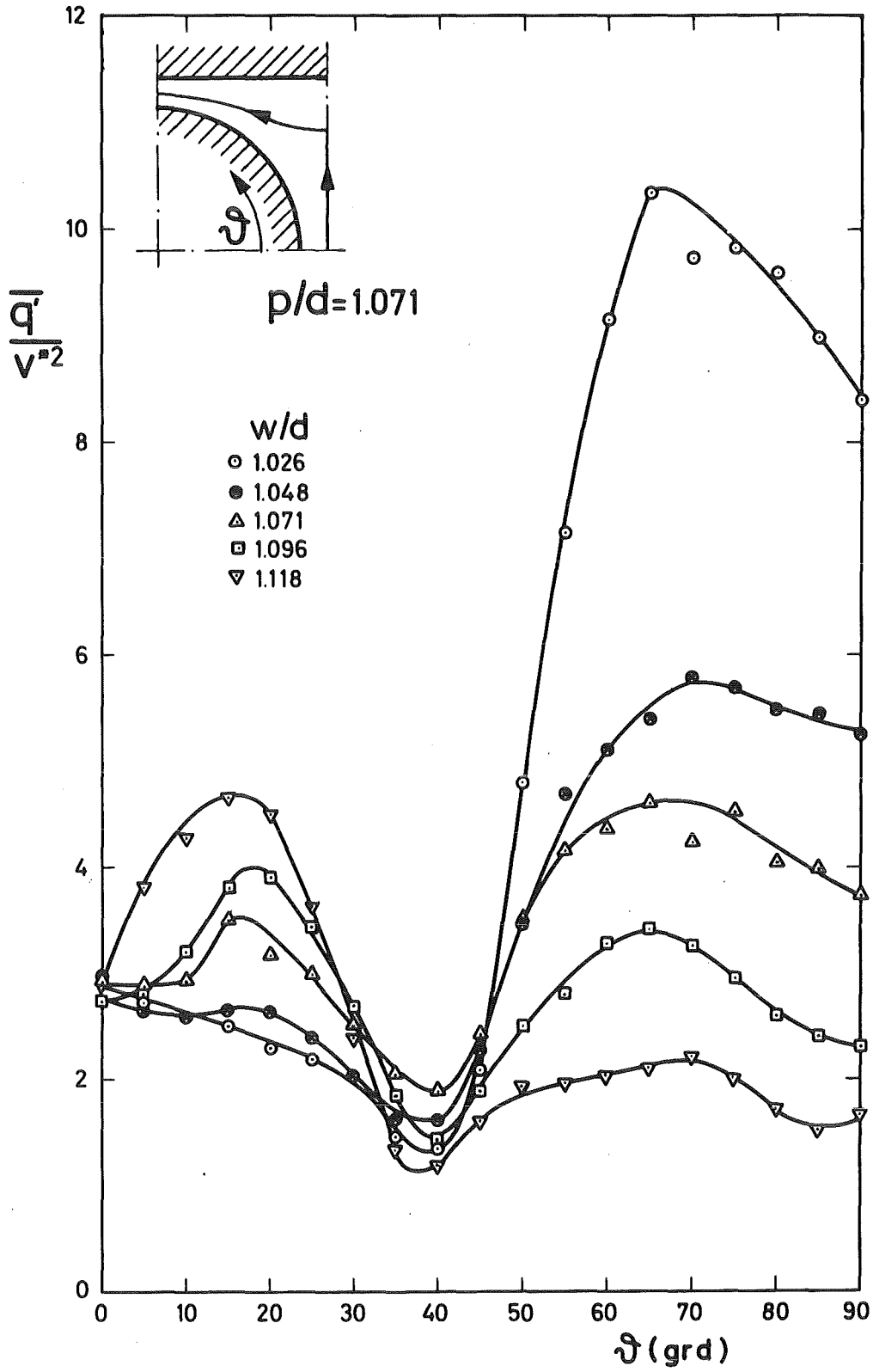
Fig. 16 Kinetic energy of turbulence along the line of maximum velocity
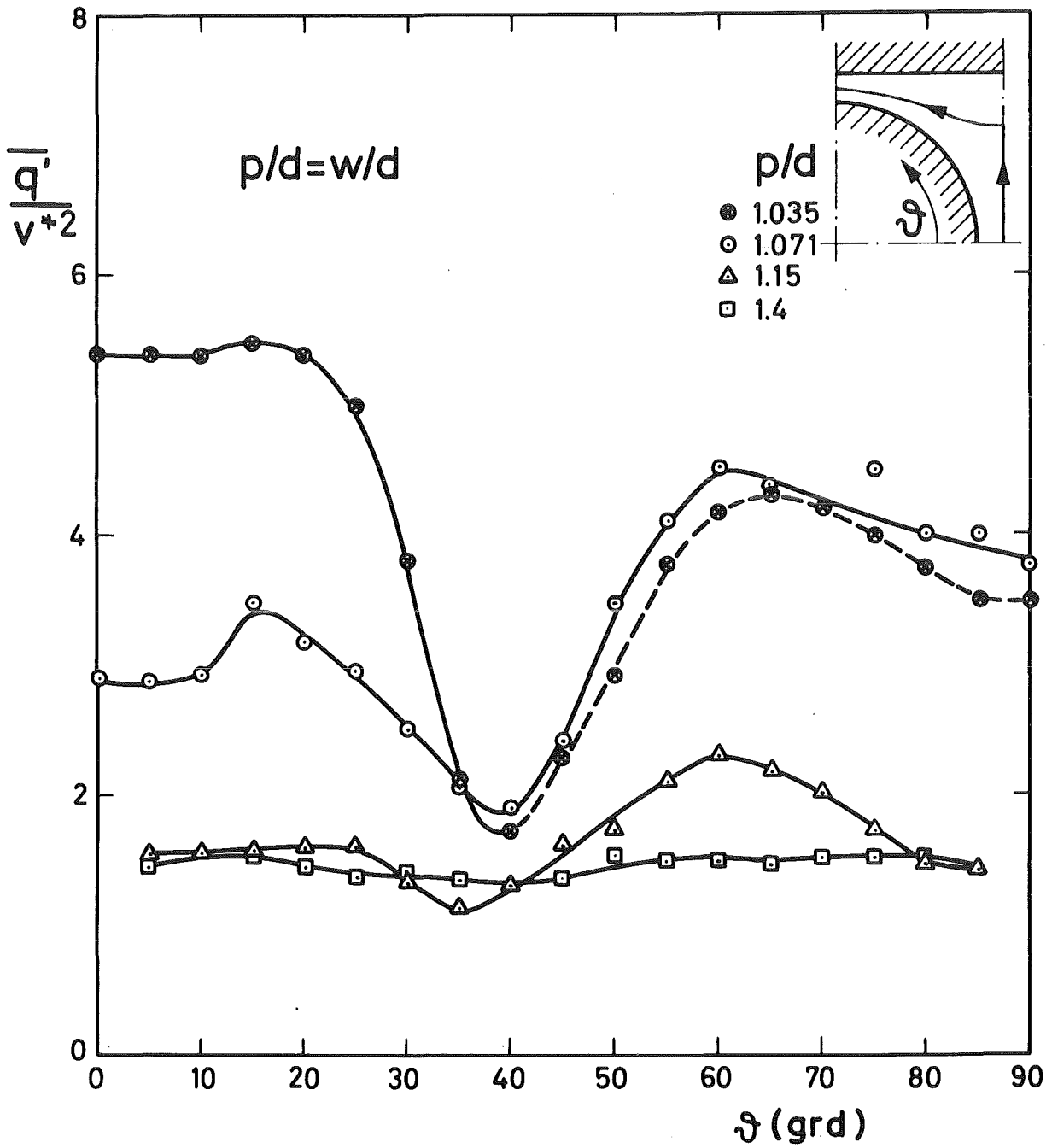
Fig. 17 Kinetic energy of turbulence along the line of maximum velocity
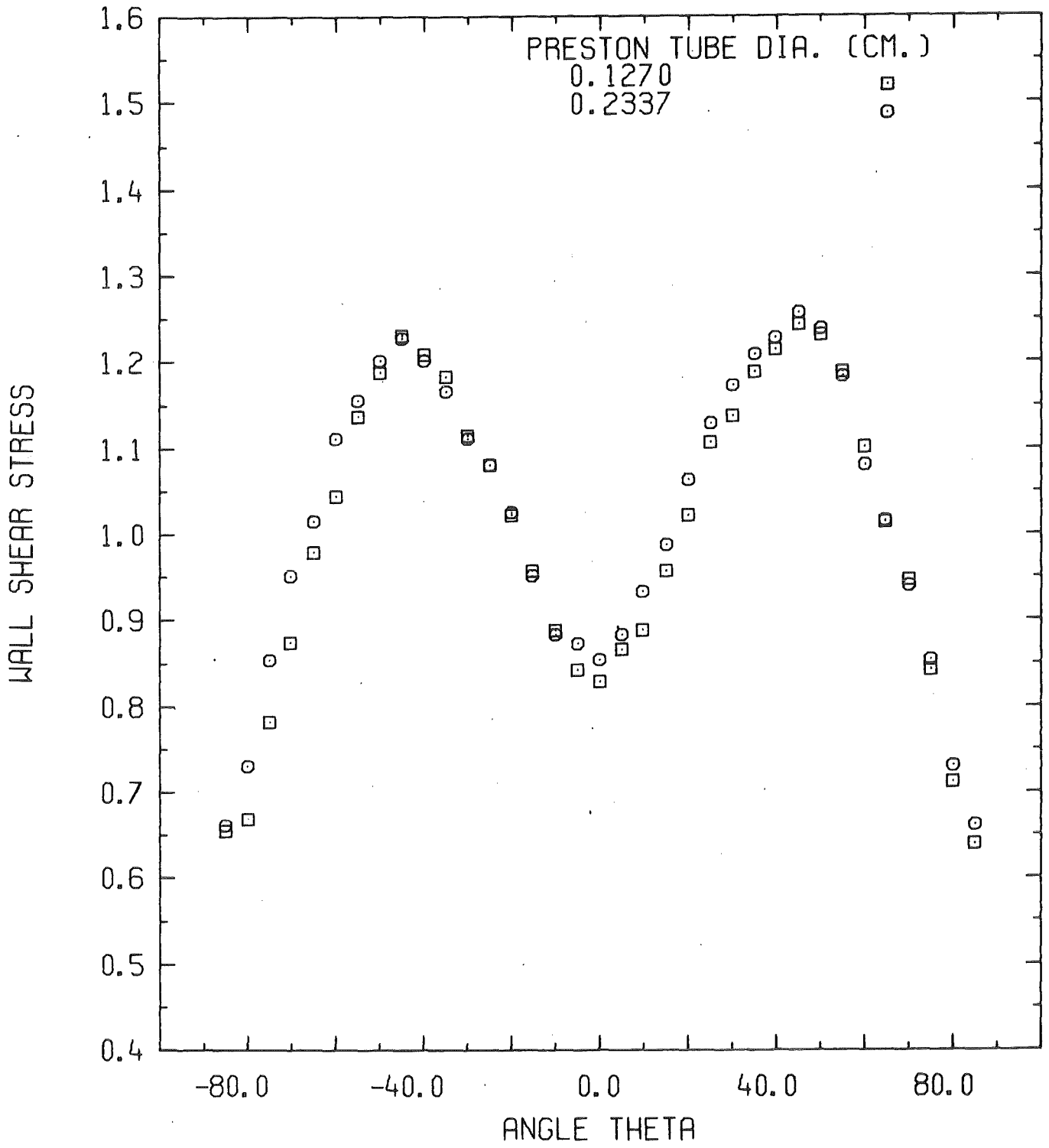
Fig. 18   Wall shear stress distribution

REYNOLDS NO. 46300

LAW OF WALL _____

ANGLE THETA

✳	10
+	5
✕	0
□	− 5
○	− 10
◇	− 15
△	− 20

A CONSTANT OF 2.0 IN U+ DISPLACES
SUCCESSIVE VELOCITY PLOTS.

DIMENSIONLESS VELOCITY U+(R,THETA)

DIMENSIONLESS WALL DISTANCE Y+

Fig. 19 Nondimensional velocity profiles in the gap

Fig. 20   Axial turbulence intensity in the gap

Fig. 21 Radial turbulence intensity in the gap
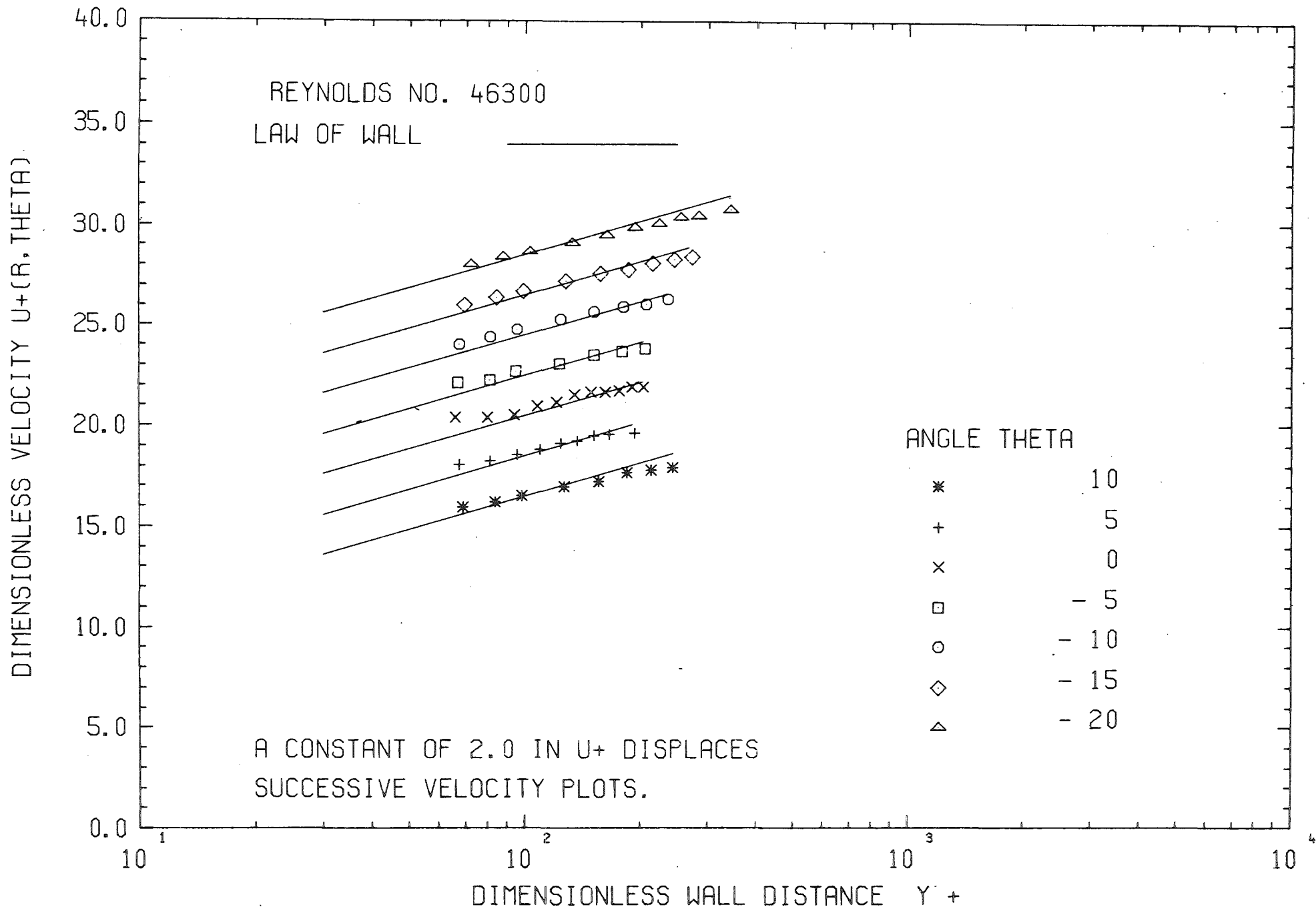
REYNOLDS NO. 46300 P/D = 1.107

Fig. 22 Azimuthal turbulence intensity in the gap
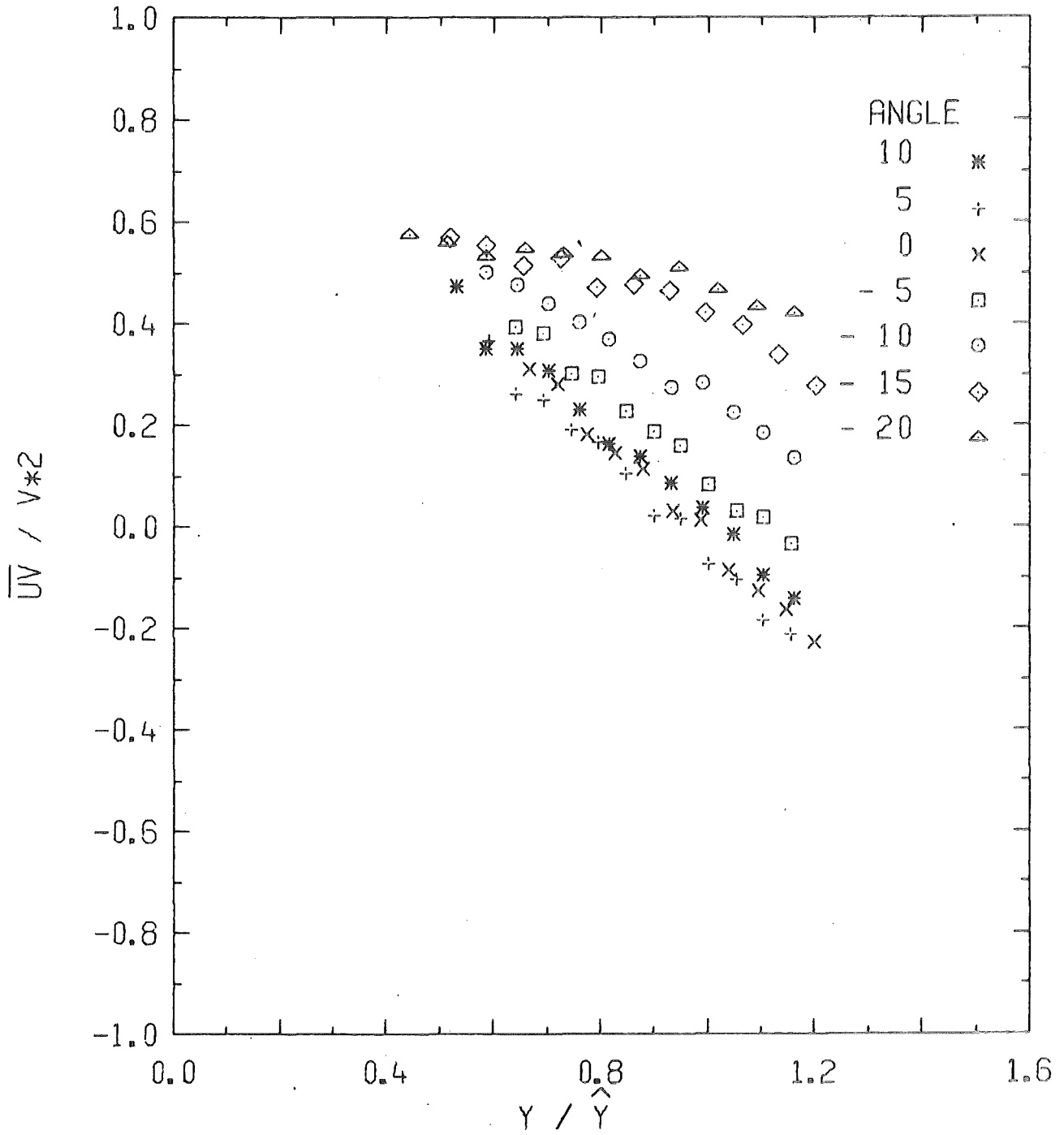
Fig. 23 Radial shear stress in the gap
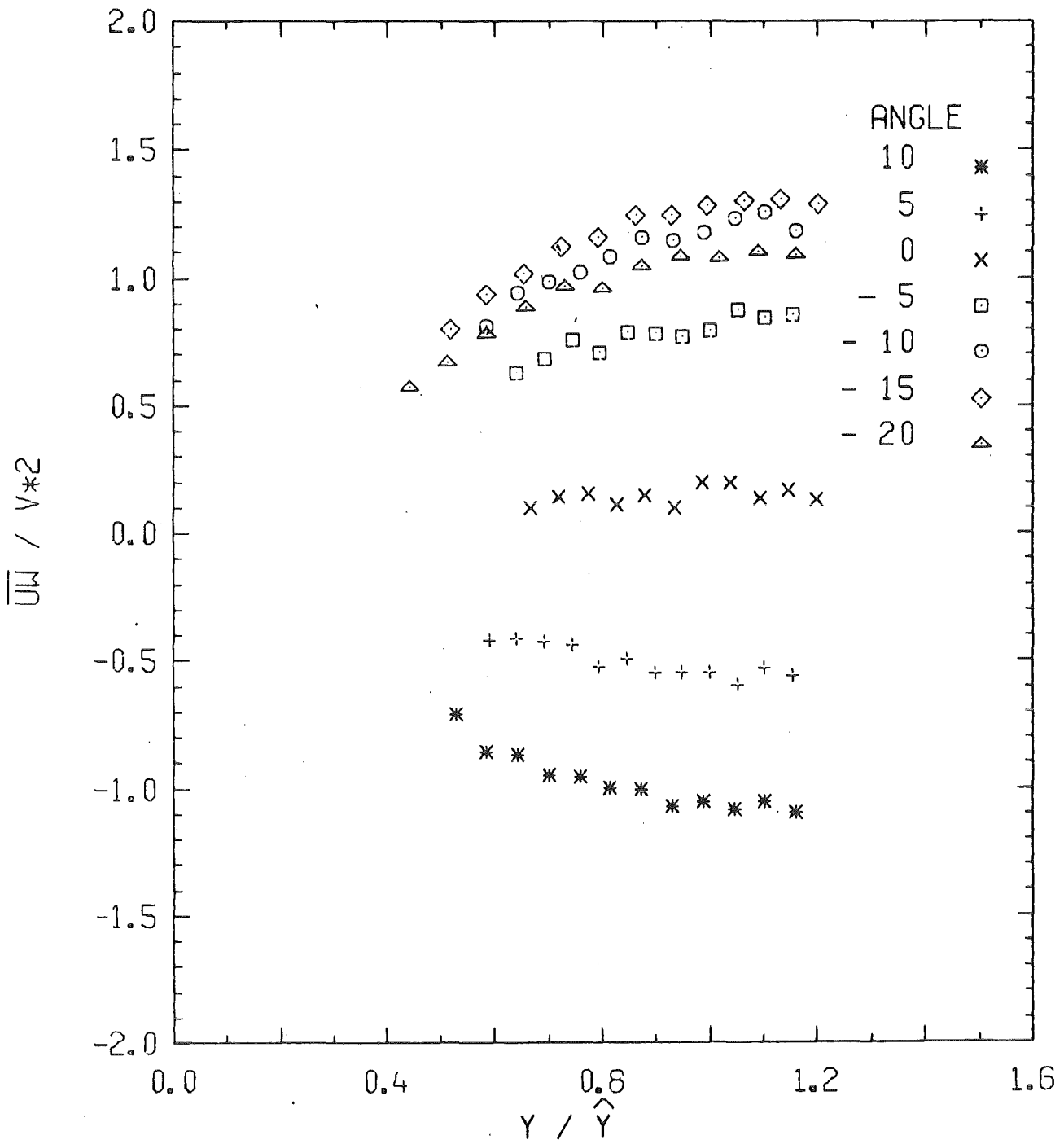
Fig. 24   Azimuthal shear stress in the gap
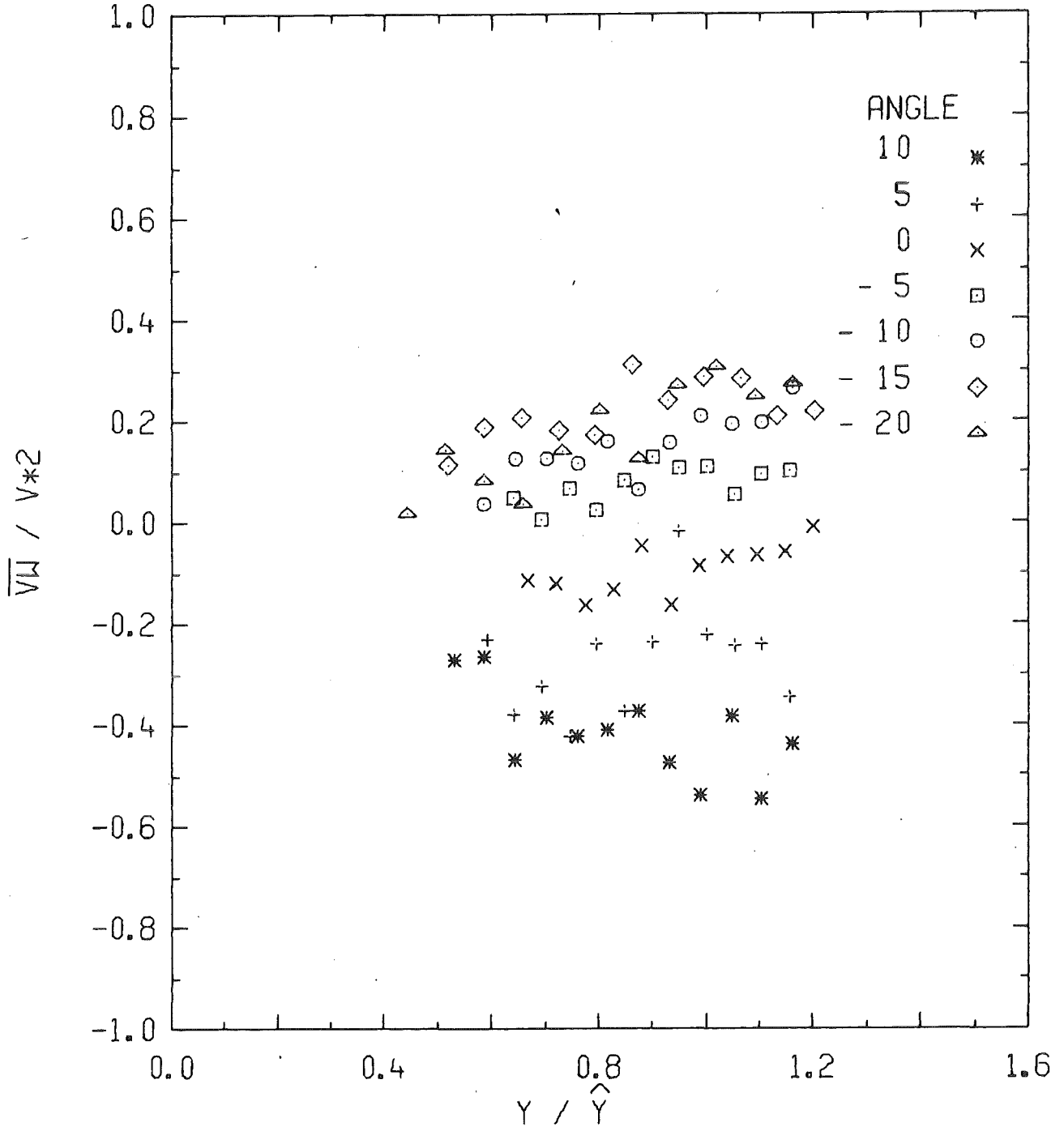
Fig. 25 Planar shear stress in the gap

$$p/d=1.036$$

$$w/d=(1+g/d)$$
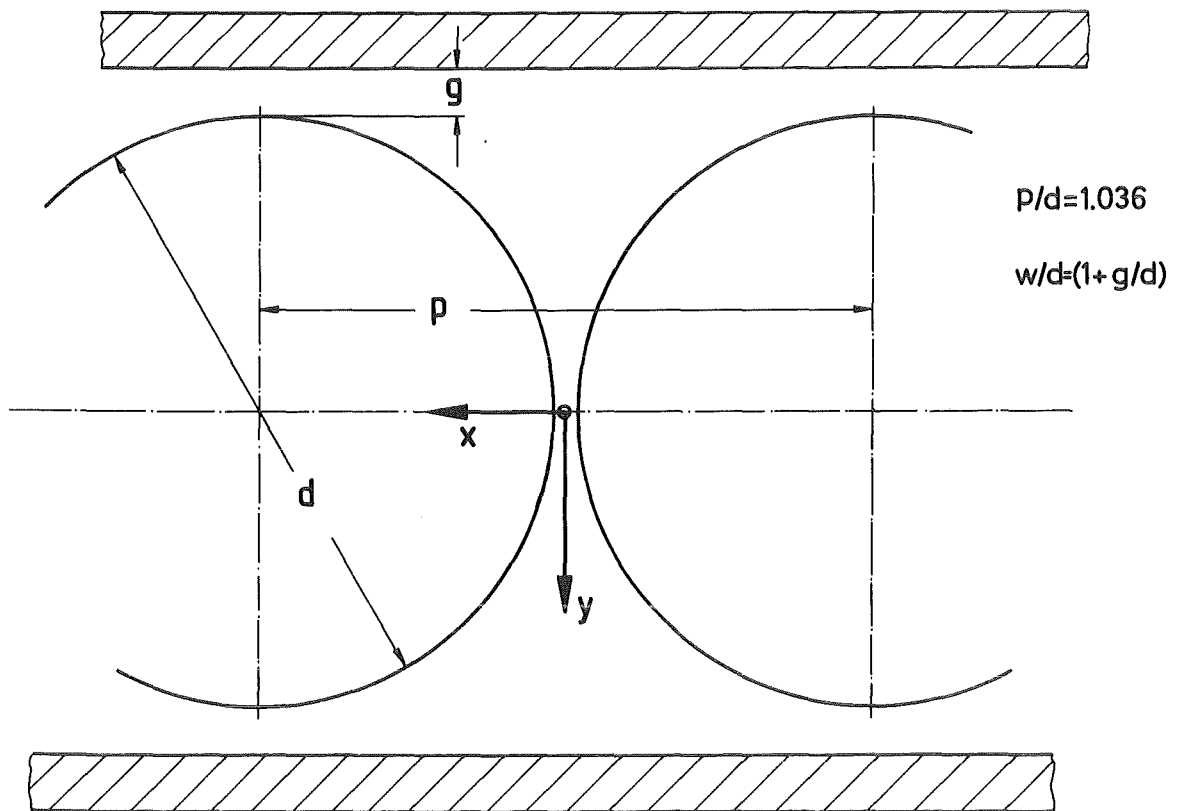
Fig. 26 Co-ordinate system used for correlation measurements
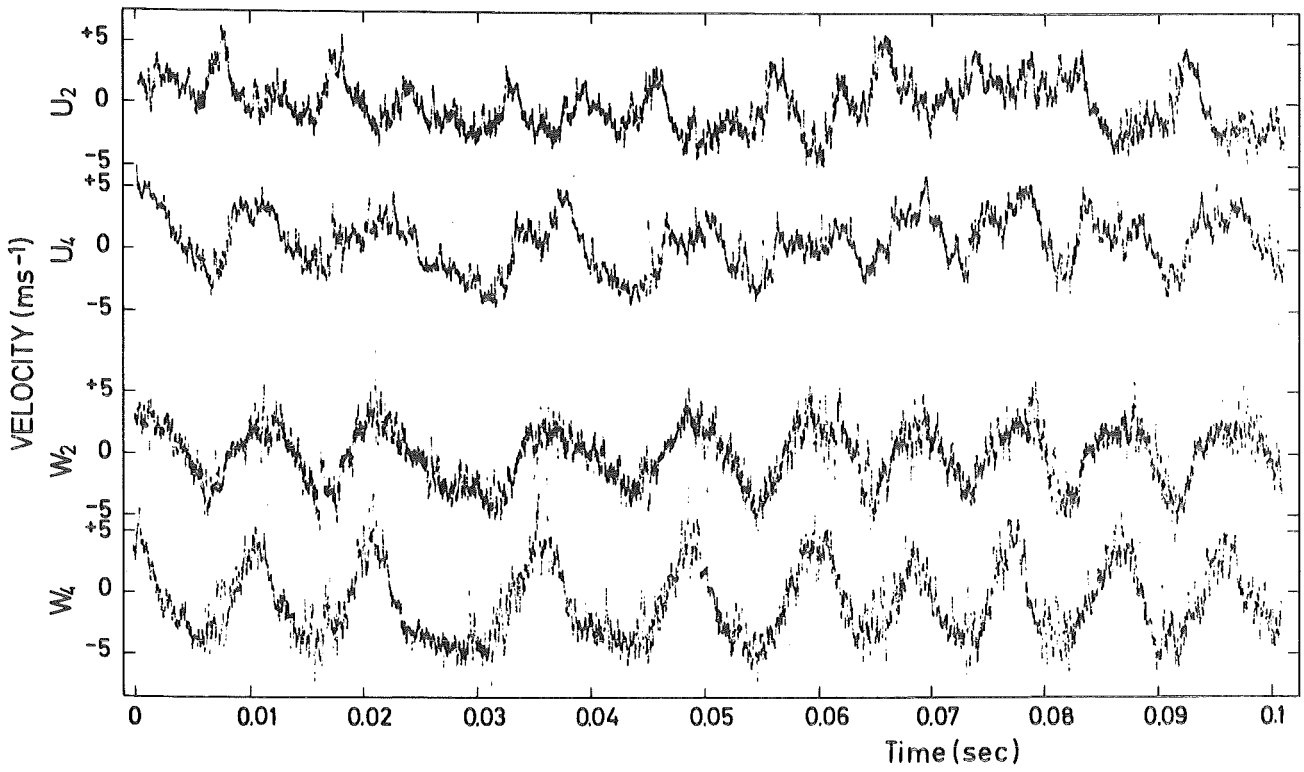
Fig. 27a   Turbulent velocity components in the x-z plane
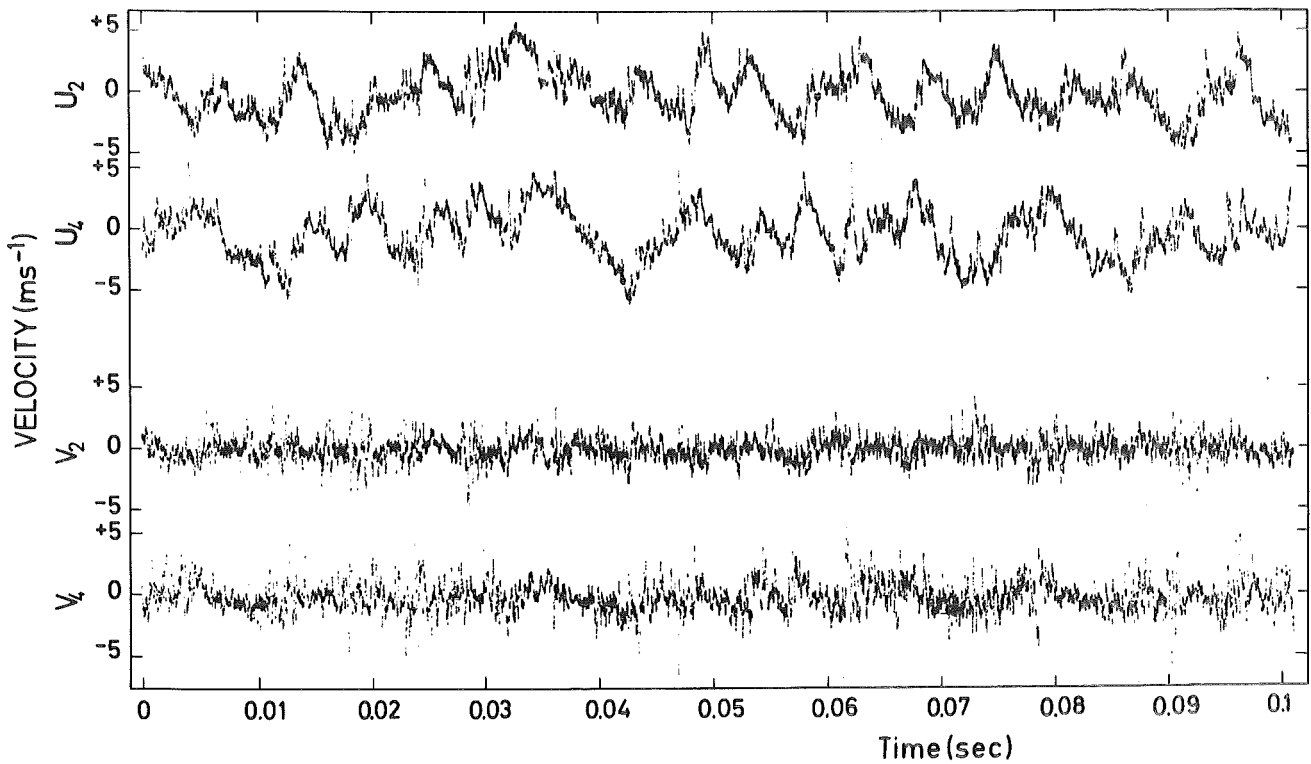
Fig. 27b   Turbulent velocity components in the y-z plane
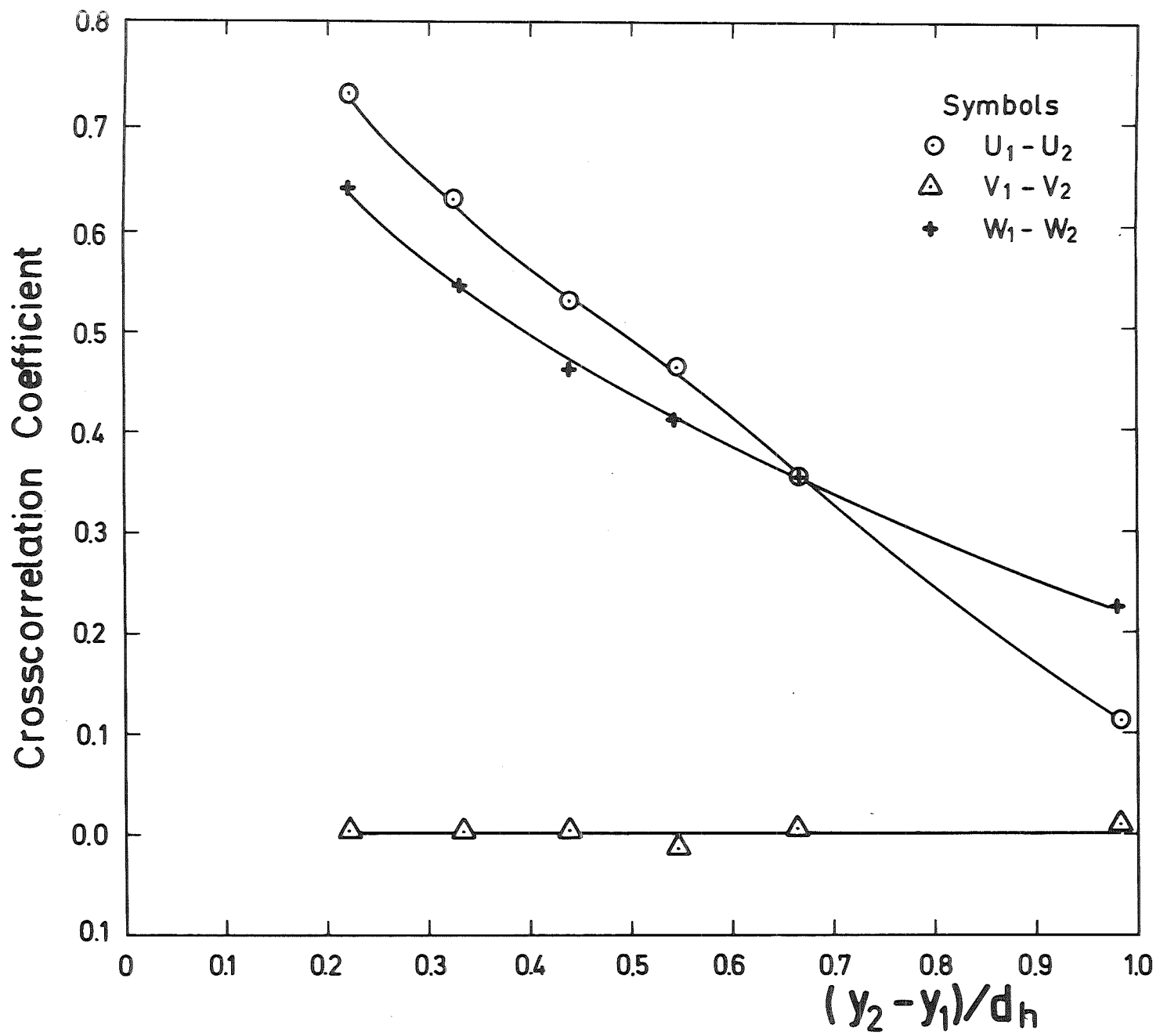
Fig. 28 Cross-correlation coefficient along subchannel
centre line
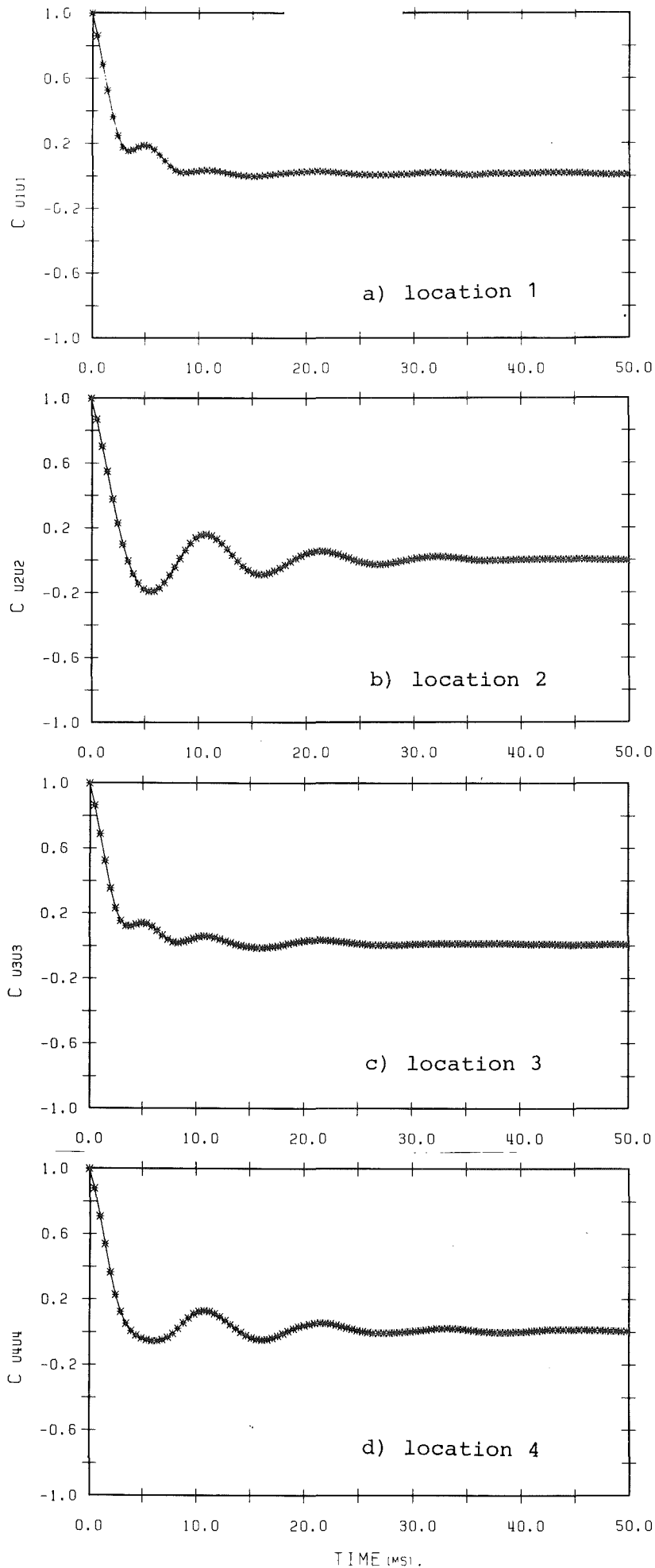
Fig. 29 Axial turbulent velocity auto-correlation

Fig. 30 Transverse turbulent velocity auto-correlation

a) locations 1, 2, axial velocity

b) locations 2, 4, axial velocity

c) locations 1, 2, transverse velocity

d) locations 2, 4, transverse velocity

TIME (MS).
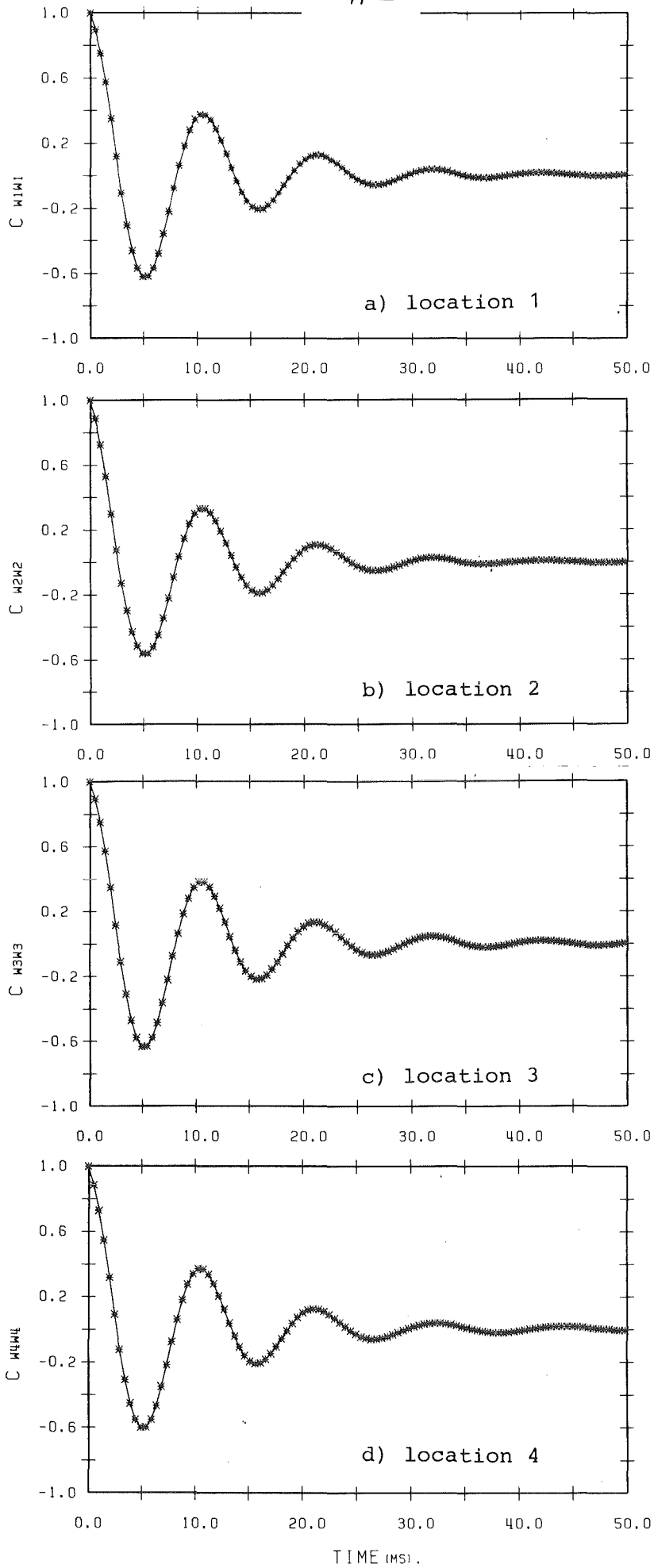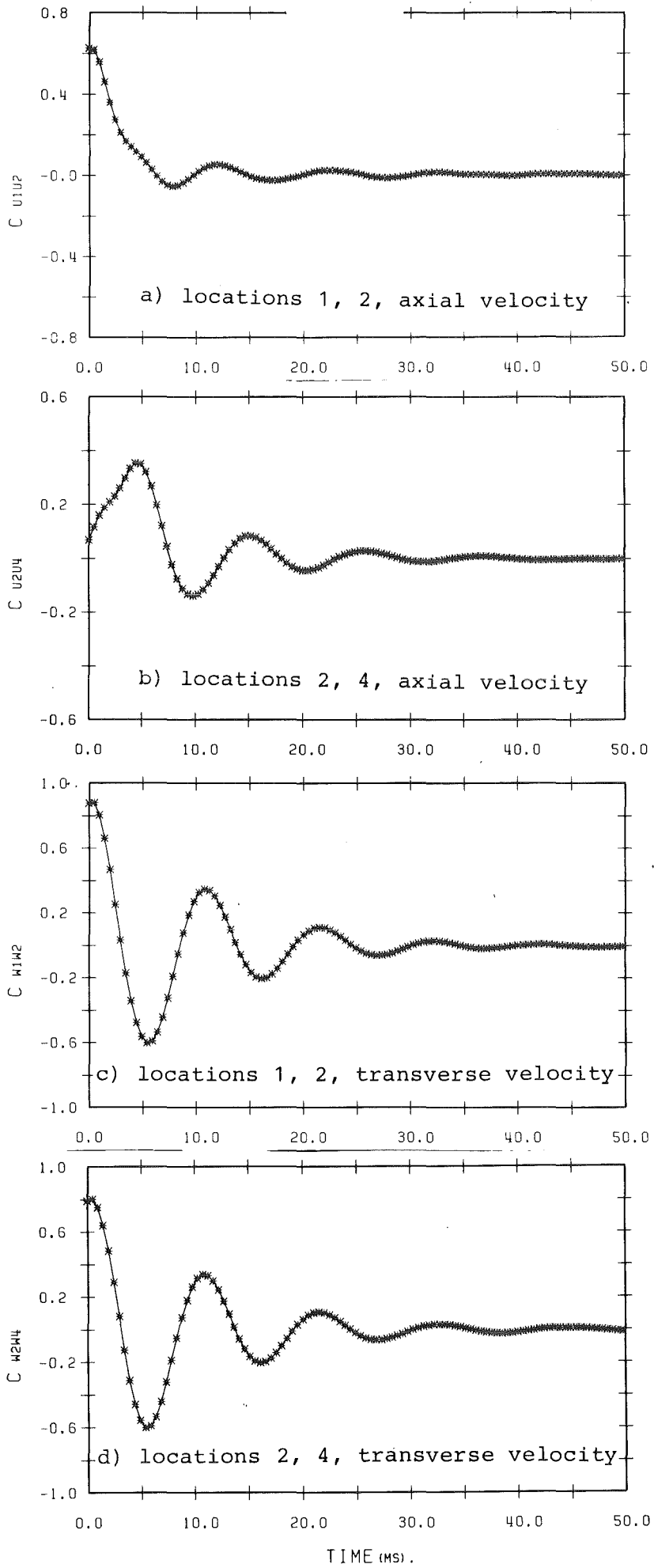
Fig. 31 Spatial cross-correlation functions

Fig. 32   Cross-correlation C_{uw}

a) axial velocity

b) transverse velocities
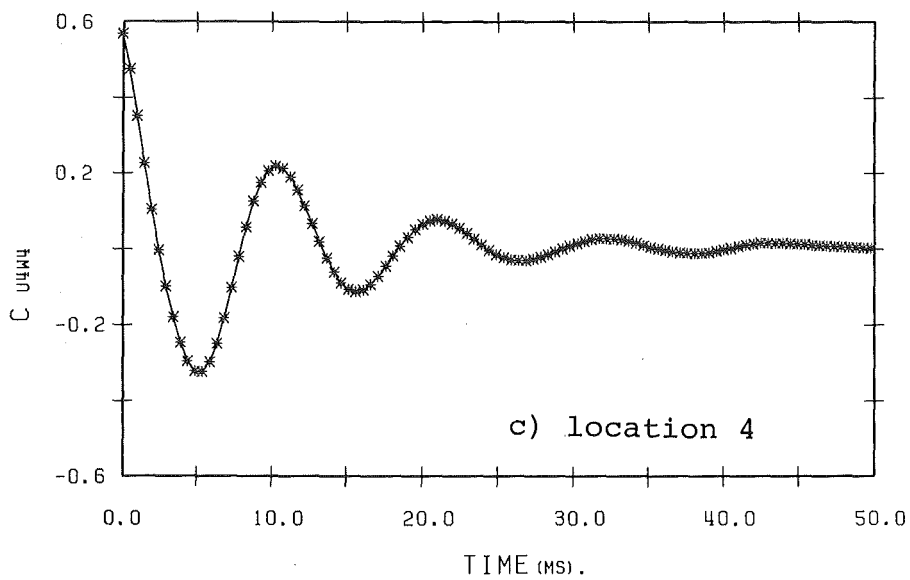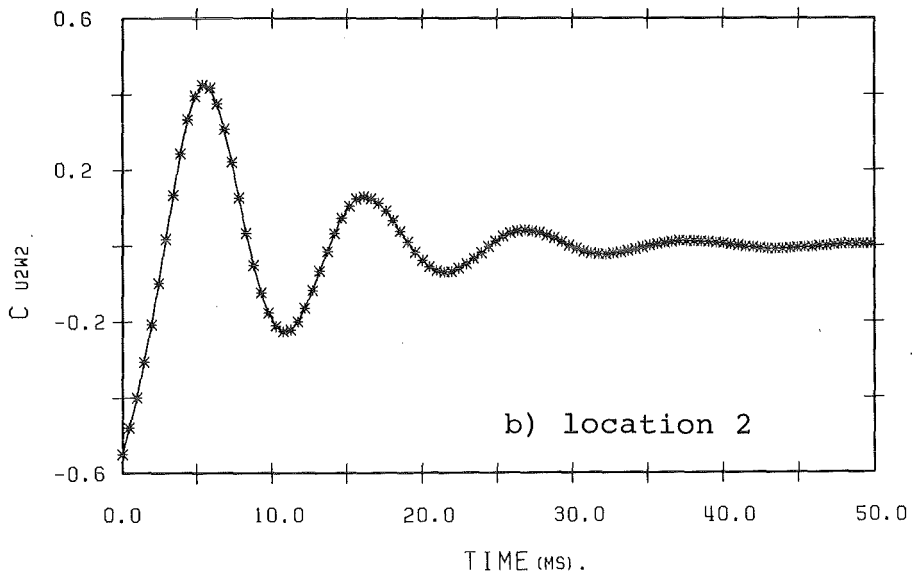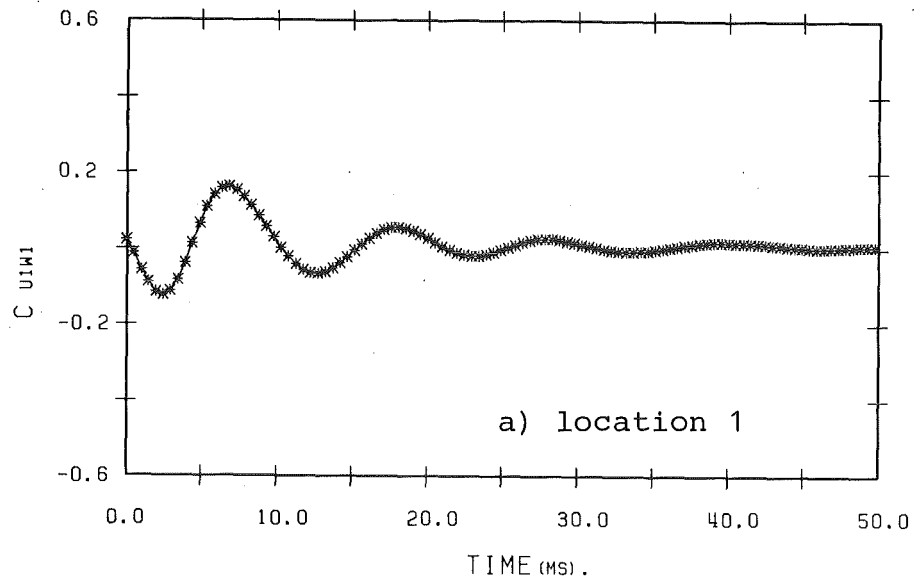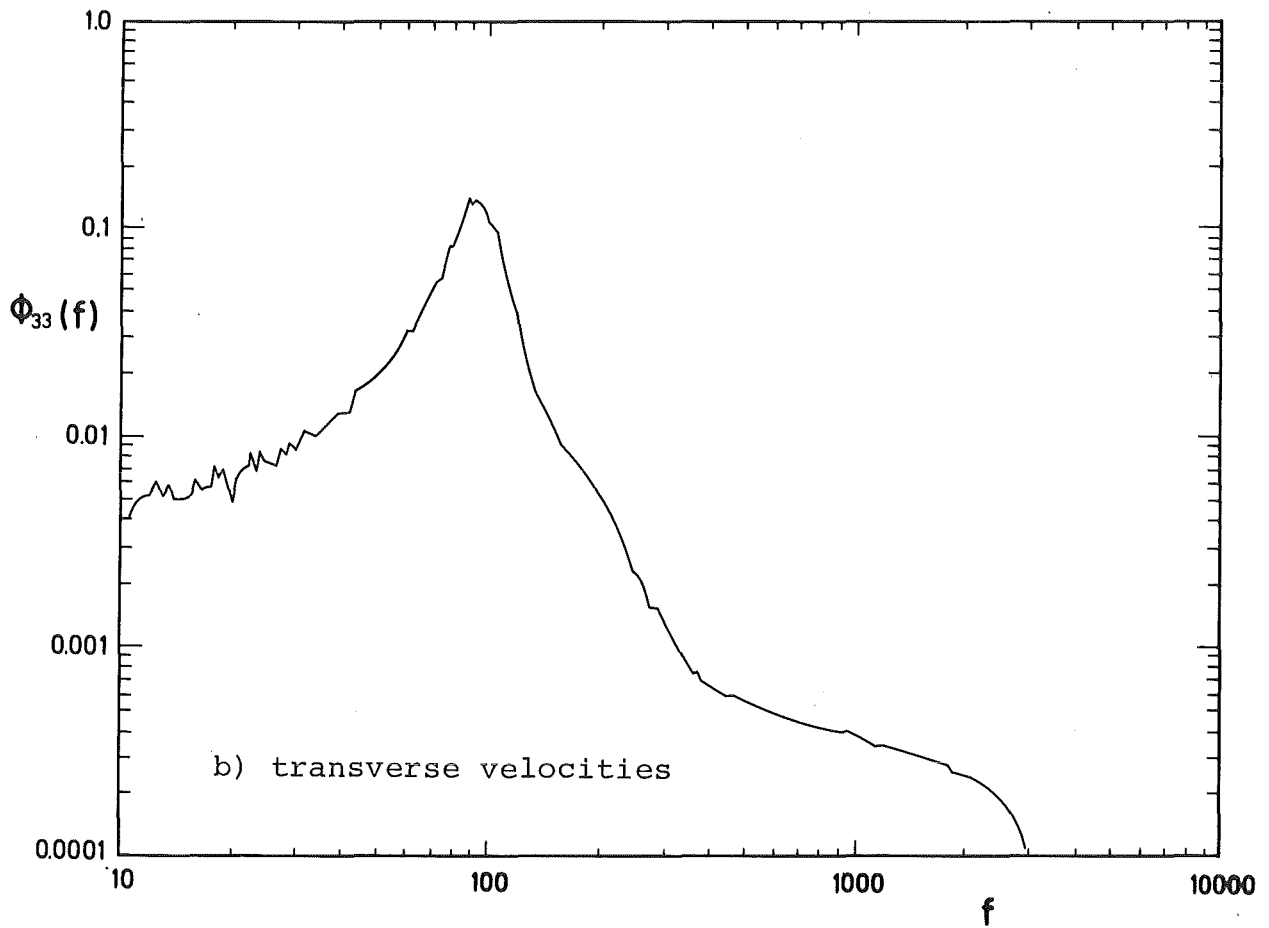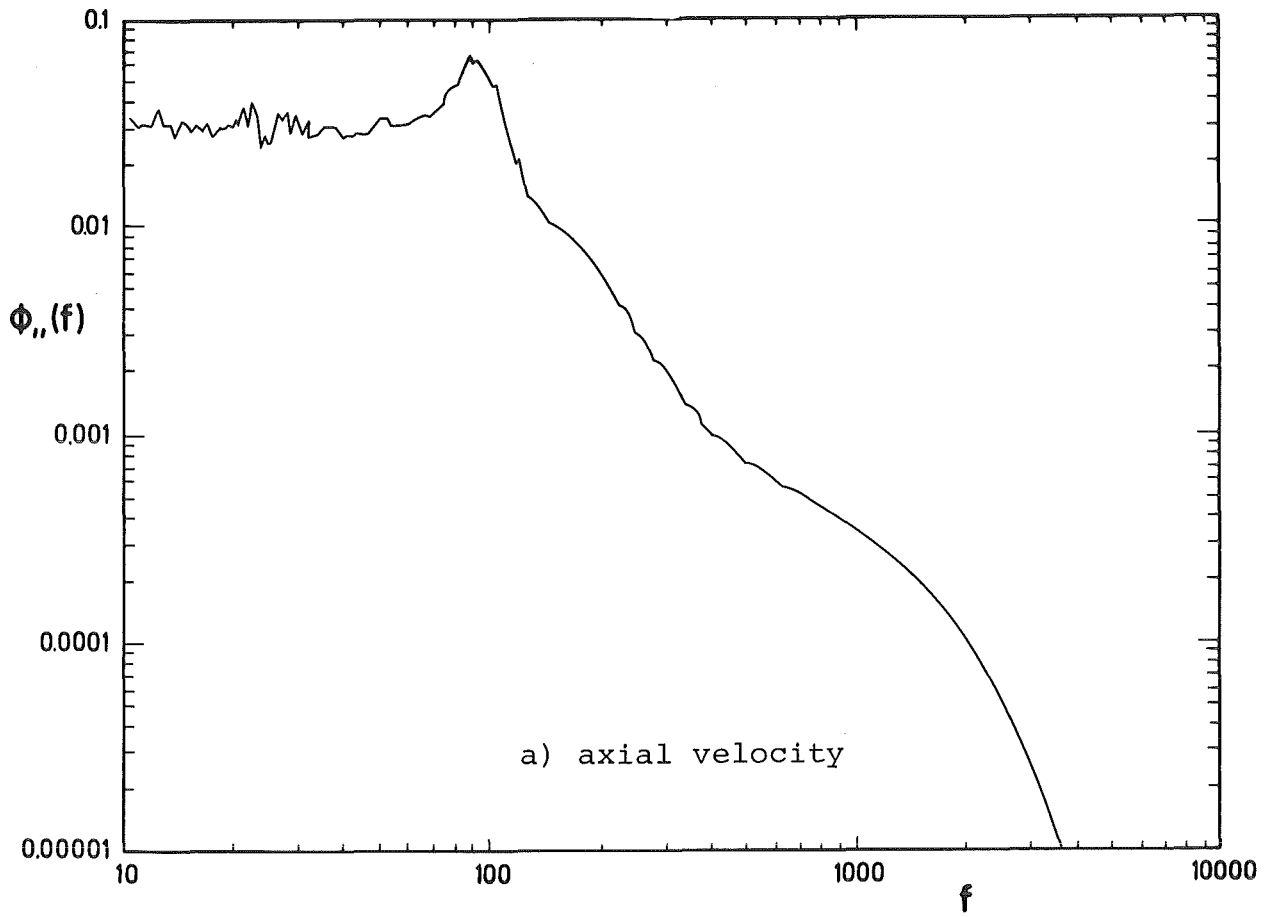
Fig. 33 Power spectra
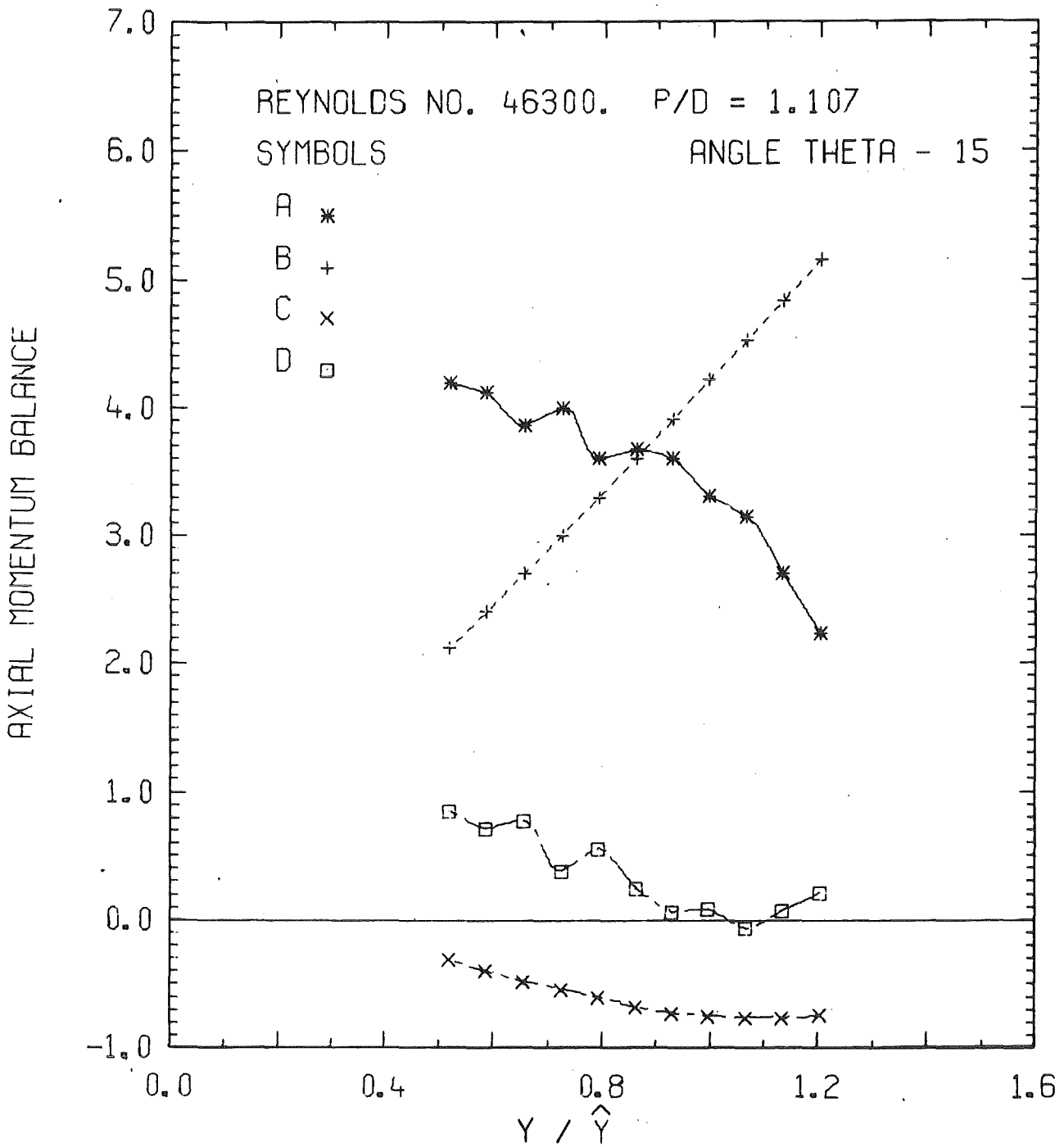
Fig. 34a   Axial momentum balance
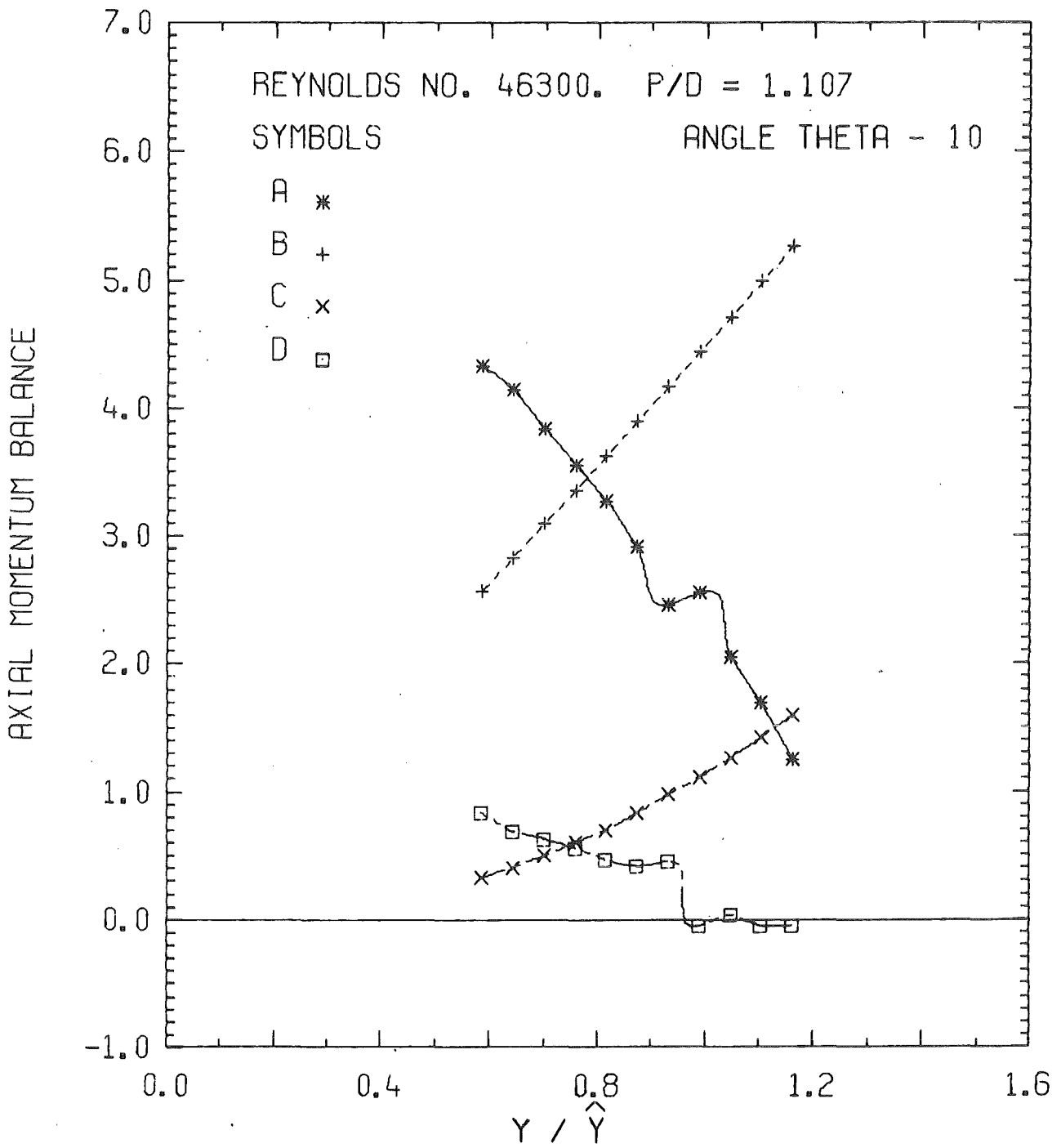
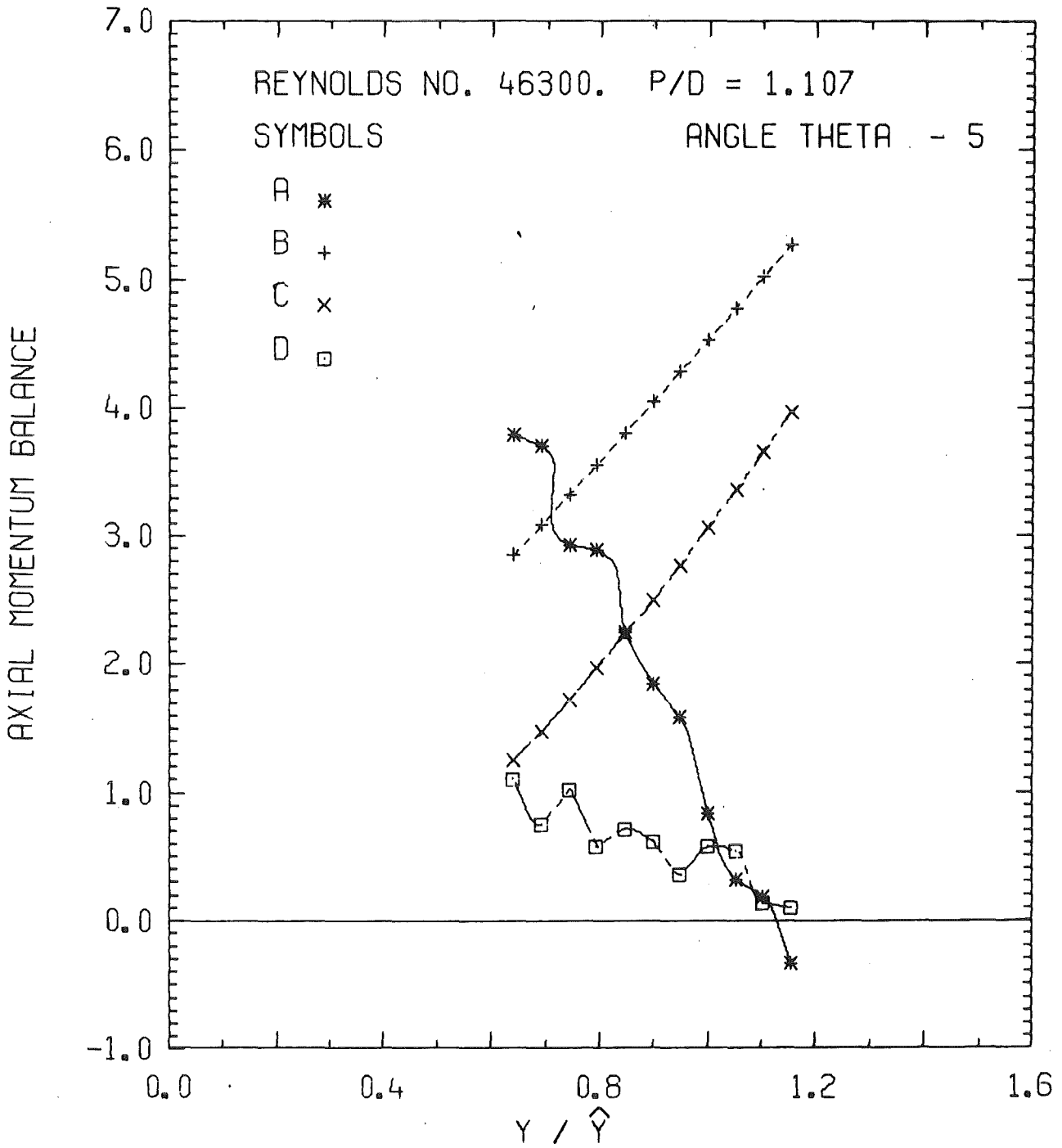Fig. 34b   Axial momentum balance

Fig. 34c Axial momentum balance

Fig. 34d   Axial momentum balance

Cyclic w velocity
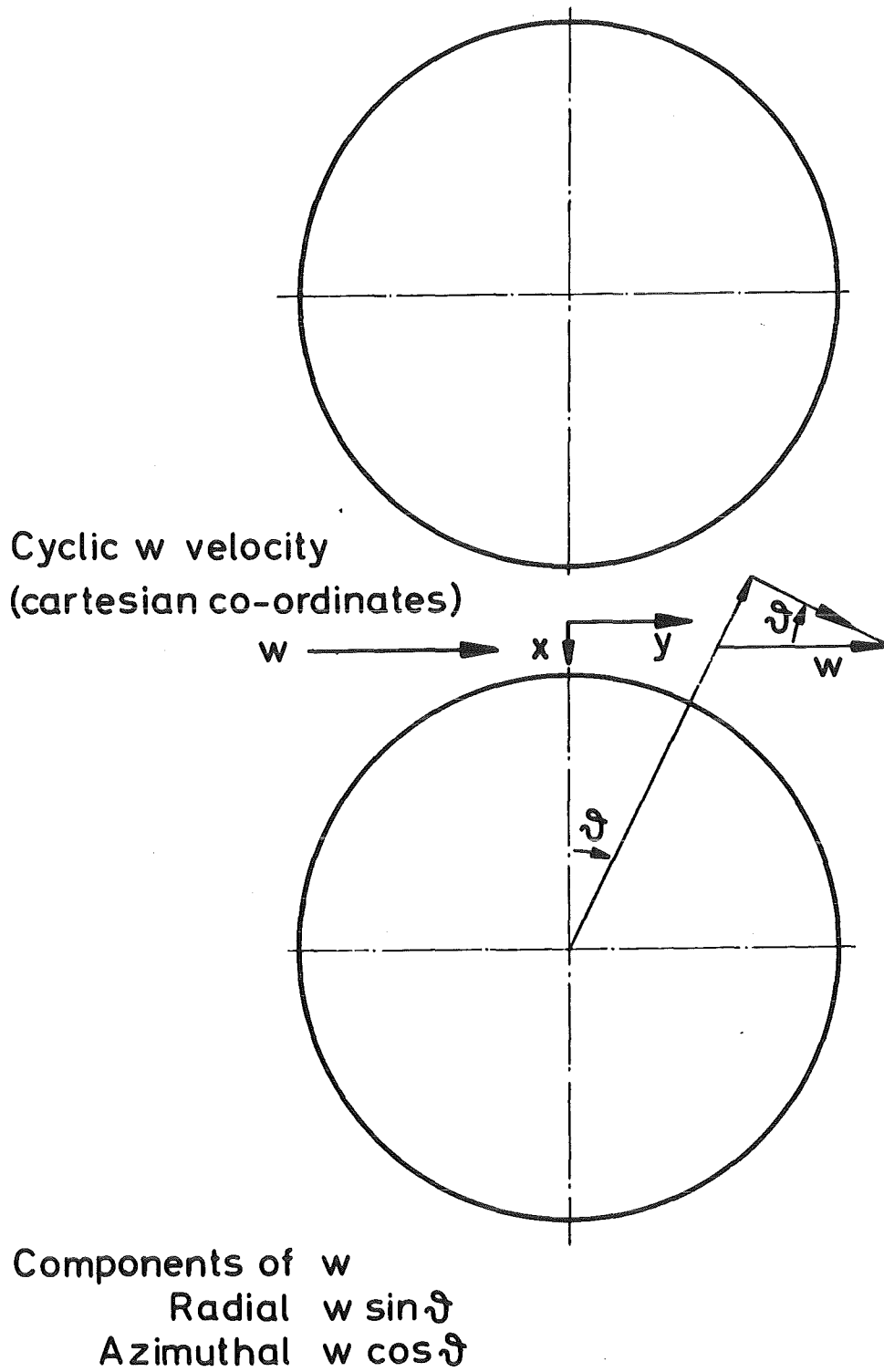(cartesian co-ordinates)

Components of w
  Radial $w \sin \vartheta$
  Azimuthal $w \cos \vartheta$

Fig. 35 Co-ordinate system